PROCEEDINGS A

royalsocietypublishing.org/journal/rspa

Research

Check for updates

Article submitted to journal

Subject Areas:
Geodynamics, Seismology, Geochemistry

Keywords:
Mantle circulation models, Seismology, Geochemistry, Geomagnetism and Paleomagnetism, Surface Deflection and Geoid, Geothermometery

Author for correspondence:
J. Huw Davies
e-mail: daviesjh2@cardiff.ac.uk

How to assess similarities and differences between mantle circulation models and Earth using disparate independent observations

J. H. Davies[1], J. Panton[1], I. Altoe[2], M. Andersen[1], P. Béguelin[1], A. Biggin[3], C. Davies[4], T. Elliott[2], Y. A. Engbers[3,10], V. M. Fernandes[5,11], A. M. G. Ferreira[6], S. Fowler[2], S. Ghelichkhan[7], B. J. Heinen[2], P. Koelemeijer[8], F. Latallerie[8], W. Li[9,12], G. Morgan[1], S. J. Mason[4], R. Myhill[2], A. Nowacki[4], C. P. O'Malley[5,13], A. Plimmer[1], D. Porcelli[8], N. Récalde[1], G. G. Roberts[5], J. B. Rodney[2], J. Shea[9], O. Shorttle[9], W. Sturgeon[6], A. M. Walker[8], J. Ward[4,14] and J. Wookey[2]

[1]School of Earth and Environmental Sci., Cardiff Univ.
[2]School of Earth Sciences, Univ. of Bristol
[3]Dept. of Earth, Ocean and Ecological Sci., Univ. of Liverpool
[4]School of Earth and Environment, Univ. of Leeds
[5]Dept. of Earth Sci. & Engineering, Imperial College London
[6]Dept. of Earth Sciences, Univ. College London
[7]RSES, Australian National Univ.
[8]Dept. of Earth Sciences, Univ. of Oxford
[9]Dept. of Earth Sciences, Univ. of Cambridge
[10] Now at Em.Sign.Prop., TNO, The Netherlands
[11] Now at GFZ, Potsdam, Germany
[12]Now at Dept. of Earth Sciences, Univ. of Hong Kong
[13]Now at Cathie Group, Newcastle upon Tyne, U.K.
[14]Now at HMRC, Leeds, U.K.

THE ROYAL SOCIETY PUBLISHING

Mantle circulation in the Earth acts to remove heat from its interior and is thus a critical driver of our planet's internal and surface evolution. Numerical mantle circulation models (MCMs) driven by plate motion history allow us to model relevant physical and chemical processes and help answer questions related to mantle properties and circulation. Predictions from MCMs can be tested using a variety of observations.

Here, we illustrate how the combination of many disparate observations leads to constraints on mantle circulation across space and time. We present this approach by first describing the setup of the example test MCM, including the parameterisation of melting, and the methodology used to obtain elastic Earth models. We subsequently describe different constraints, that either provide information about present-day mantle (e.g. seismic velocity structure and surface deflection) or its temporal evolution (e.g. geomagnetic reversal frequency, geochemical isotope ratios and temperature of upper mantle sampled by lavas). We illustrate the information that each observation provides by applying it to a single MCM. In future work, we will apply these observational constraints to a large number of MCMs, which will allow us to address questions related to Earth-like mantle circulation.

1. Introduction

Our planet's evolution and present-day state is ultimately driven by convection in its deep interior. This convection is partially controlled by subducting slabs at destructive plate margins, and partially by thermal upwellings initiated at thermal boundary layers. While the locations of cool subducting slabs and hot plumes are reasonably well constrained close to the surface of the Earth, their positions, morphologies and time-dependent behaviour in the lower mantle remain poorly constrained.

Models of global mantle convection can now include phase transitions, coupling between composition and density, compositional tracking, decompression melting and surface motions driven by plate history models. The predictions of these simulations over recent Earth history to present-day can be tested with disparate observations that can help to constrain mantle flow. Such work has been done over the last two decades with increasing sophistication, primarily focusing on seismic and surface topography observations for constraints (e.g. [1–11]).

In this paper we demonstrate how suites of observations—with different sensitivities to the spatio-temporal evolution of the mantle—can be used to test predictions from MCMs (see Figure 1). The specific constraints used here have been selected with the goal of providing a broad coverage of this 4D space, something that will ultimately give the best chance of constraining MCMs. These observations come from a wide range of disciplines, including seismology, surface deflections, geomagnetism, petrology and geochemistry. We first present the simulation method. We then, in turn, discuss the geophysical or geological context of each observation, together with the relevant predictions from an actual MCM (case m_cc_066_u) for that observation. We note that this MCM is a not very Earth-like sample model and that our constraints are not exhaustive; many other observations could be used, e.g. hiatus maps, body-wave traveltimes [12] and lithospheric stress field (see other contributions to this special issue). What is novel here is both some of the individual constraints and the breadth of constraints applied simultaneously.

2. Mantle Circulation Modelling

Our mantle circulation models (MCMs) use models of recent plate motion history as surface velocity boundary conditions. This gives plate tectonic-like surface velocities in locations consistent with geological history on Earth [1–6,14,15]. Predictions from the MCMs enable geographic comparisons. This includes comparisons with observations that are independent of horizontal surface motions. Our long-term goal is to use such comparisons to constrain the

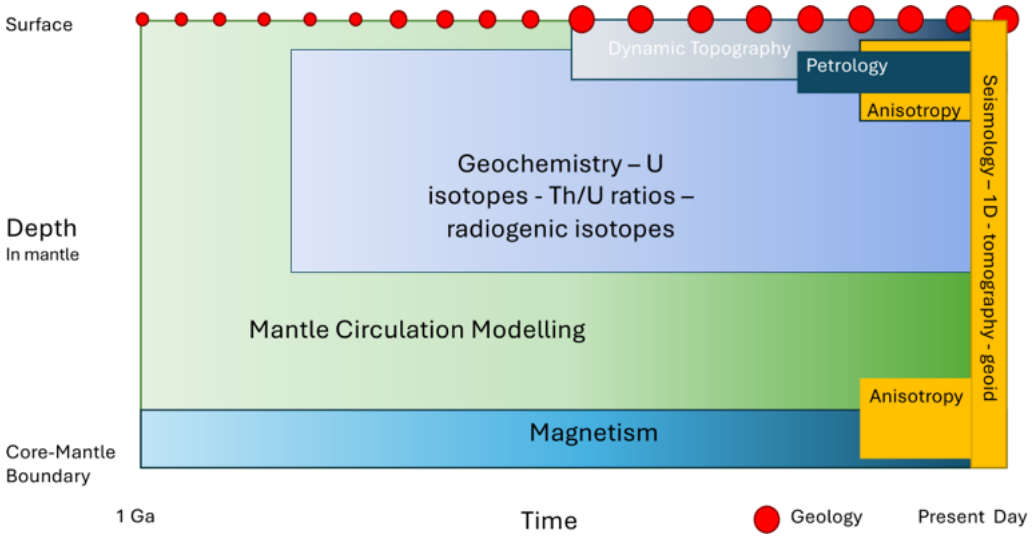

Figure 1. Schematic showing where in space (illustrated schematically over mantle depth) and time we might expect different constraints and models to constrain global mantle circulation. The size of geology symbols reflects number of observations while the shading hints at likely sensitivity of constraint. Different aspects of seismology will constrain different depths, e.g. fundamental mode surface wave data primarily constrain the shallow mantle, while Stoneley modes add constraints about the lower mantle. Some aspects like dynamic topography and geoid can have specific sensitivity kernels that this figure cannot represent. Inspired by [13].

properties of the mantle, for example the viscosity of the mantle and the density of recycled oceanic crust. A better understanding of its viscosity, which controls the rate of flow of the mantle, would for example allow one to address the question of how quickly slabs sink in the mantle [16]. Knowledge of the density of recycled metamorphosed oceanic crust, which controls how/if it segregates from the bulk flow, would allow one to address the question to what extent does recycled oceanic crust contribute to the Large Low Seismic Velocity Provinces (LLSVP) of the lowermost mantle [17].

We simulate mantle dynamics by solving the conservation of mass, momentum, energy and composition equations in global 3D spherical geometry, following [18–22]. Details of our MCM modelling are presented in the supplemental material (SM, Table SM.1), with a brief summary presented here. The simulation presents a compressible mantle, assuming an anelastic approximation using a Murnaghan equation of state (see Bunge *et al.* for details [20], with a depth-varying coefficient of thermal expansion and reference density). The lateral surface velocities arise from the plate motion history of Müller *et al.* [23], applied from 1 Ga to present-day in 1 Myr steps, scaled to the natural velocity of the model, avoiding forced convection. We also ensure zero surface radial velocities, while the core-mantle boundary velocity boundary condition is free-slip. The surface and core mantle boundary are isothermal, with the surface kept at 300 K, while notably, the temperature of the core evolves self consistently over time using the coupled model of Davies [24]. The resulting CMB heat flux evolution is presented in SM, Figure SM.2

The model is thermochemical and tracks bulk composition using a single parameter, C, which varies from $C = 0$ (harzburgite-like), through $C = 0.2$ (lherzolite-like) to $C = 1$ (basalt like), advected on particles. For simplicity, we will use the terms harzburgite, lherzolite and basalt to represent these compositions, even in regions of the mantle where the mineralogy is changed and these terms do not strictly apply. The basalt is assumed to be denser than the average mantle in the lower mantle (buoyancy number = 0.66; see SM). It is less dense between 660 km and 720 km to mimic the delayed phase transformations in the basalt component, which some have argued

can produce a basalt barrier [25]. The model includes the dynamic influence of phase boundaries at 410 km and 660 km depth (see SM). We also implement self-consistent melting following Van Heck *et al.* [22] when the source temperature exceeds its solidus. This produces a surface layer enriched with basalt, which is recycled into the mantle in regions of plate convergence. The melting also considers partitioning of tracked elements according to their partition coefficient and the degree of melting. The tracked elements include the heat producing radiogenic isotopes and their daughters (Th, U, K, Pb, He, Ar).

The rheology of the mantle is assumed to have a temperature-dependent Newtonian viscosity. The radial reference profile includes a lower viscosity in the upper mantle (4×10^{21} Pas), a higher viscosity in the lithosphere ($\times 100$) and lower mantle ($\times 30$), which decreases to a low viscosity ($\times 1$) as we descend towards the hot core mantle boundary (Figure SM.3). The simulation presented here uses the benchmarked [21], parallel [19] code TERRA [14,18,20,22,26–28], with an average lateral resolution at mid-mantle depth of $\approx$ 45 km, with similar radial spacing.

3. Producing Isotropic Seismic Structure from Mantle Circulation Models

The outputs of the thermochemical MCMs (temperature and composition at a given pressure/computational node) serve as inputs for extracting rock physical properties from tables produced from phase equilibrium calculations, outlined below.

In general, the compositional value C on the particles and the fine mesh ($0.0 < C \leq 1.0$) correspond to enrichment relative to harzburgite. However, because only one C value is tracked, an intermediate value could correspond to a single lithology or a mechanical mixture of multiple lithologies [29]. To determine seismic velocities from P, T and C, we must therefore first make an assumption about how C maps to the local lithology. In our approach, we assume that our models are composed of mechanical mixtures of three discrete bulk compositions. If $0.0 \leq C < 0.2$, the rock is assumed to be a mixture of harzburgite and lherzolite with proportions varying linearly with the C value, otherwise it is assumed to be a linear mixture of lherzolite and basalt for $0.2 \leq C \leq 1$.

Throughout this paper, we assume that harzburgite, lherzolite and basalt have constant bulk compositions (Table SM.3), assuming the compositions reported by Baker and Beckett [30] (harzburgite), Walter [31] (lherzolite) and White and Klein [32] (basalt). The physical properties of lherzolite, harzburgite and basalt are calculated using a Gibbs free energy minimization, as implemented in Perple_X [33] using the equation of state of Stixrude and Lithgow-Bertelloni [34–36]. We use the mineral dataset provided in [36] and available at github.com/stixrude/HeFESTo_parameters_010121. This provides thermodynamic and elastic properties for each of the bulk compositions, stored as three separate P-T-property tables. As the mineral dataset lacks a covariance matrix, we cannot propagate parameter value uncertainties into uncertainties for the calculated physical properties. However, as a first-order approximation, we estimate an average uncertainty in V_s of $\sim$0.4% for harzburgite and lherzolite and $\sim$1% for basalt (see SM section 2). We expect the uncertainties in V_p to be of a similar magnitude. The effective isotropic seismic velocities for each bulk composition are corrected for anelastic effects using model Q7g [37,38], which produces a good agreement with published studies on attenuation [39]. Final effective densities and seismic velocities throughout the domain are calculated by harmonic averaging of the lherzolite, harzburgite and basalt material, weighted by the mass fractions f_i^{M} of each bulk composition (see SM).

4. Testing models with seismic observations

Seismology provides primarily a snapshot of the present state of the Earth's mantle (Figure 1), with a wide range of possible observations that can be used to test predictions of an MCM. Here,

we will present a sub-set only, to give an example of what is possible. Many of these seismic constraints have already been considered in other studies [12,40], but typically not all together.

(a) Whole mantle

(i) 1D isotropic

The 1D radially-averaged seismic structure of the Earth is an obvious choice for a metric with which to test MCMs [41]. This structure primarily depends on the bulk composition of the mantle as well as the average temperature (geotherm), properties which are usually tracked in MCMs. The conversion to seismic velocities is achieved by thermodynamic modelsets of mineral phases, which are increasingly well-constrained by inversions of high-quality experimental data [34–36,42]. The synthetic 1D structure can be readily compared to high-quality models created by inversion of seismic data [41,43] . A comparison of the radially-averaged 1D profile extracted from our example MCM with PREM [41] is shown in Figure 2. The radially averaged structure of our example MCM matches PREM well below ∼800 km depth (within 1-2%), but in the bottom ∼400 km in the mantle, the deviations from PREM increase (Figure 2). This is possibly due to the compositional gradient in the MCM, where the recycled oceanic crust preferentially collects at the base of the mantle. Such unexpected deviations can be used to identify and in future potentially reject poorly performing MCMs.

Figure 2 also highlights some of the caveats that come from a naive comparison between 1D radially-averaged velocity structure and velocity structure obtained from seismic data. The first is that the synthetic structure exhibits smooth increases in velocity around “410 km” and “660 km” depth. These smooth increases are a consequence of averaging sharp transitions that take place at different depths due to the temperature dependence of the olivine-wadsleyite and ringwoodite-breakdown reactions. The discrete jumps in the PREM and AK135 models arise because those models are built on seismic data that are sensitive to the magnitude and depths of jumps in seismic velocity, rather than 1D radial structure [44]. At depths shallower than <400 km, discrepancies are due both to the lack of continental lithosphere in the MCM, and a lack of mineralogical justification for a 220 km discontinuity proposed in PREM. It is noteworthy that the 220 km discontinuity does not exist in AK135 [43]. Further details provided in SM Sect. 3.1.1.

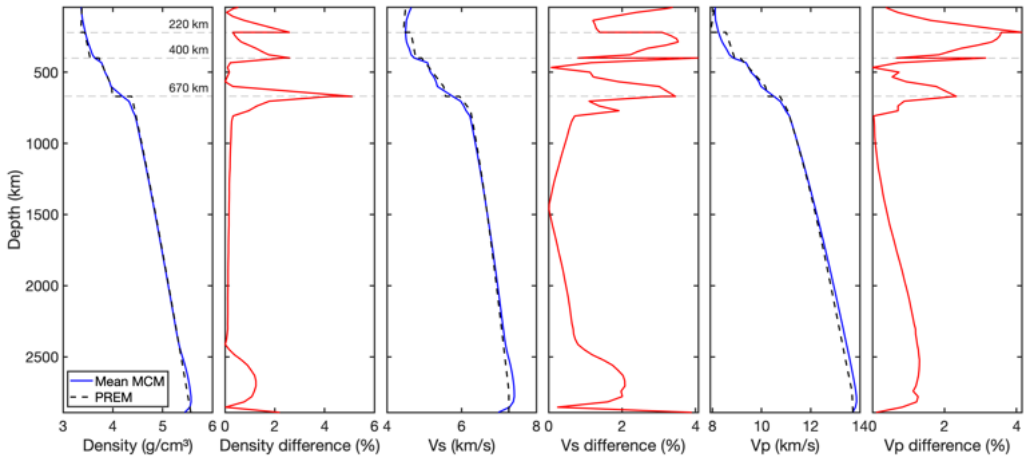

Figure 2. Comparison of the 1D average density, V_s and V_p profiles of the MCM (blue lines) compared with PREM (black dashed lines). Red lines show the absolute difference in percent between the models. Dashed horizontal lines at 220, 400 and 670 km depth represent the major seismic discontinuities in PREM.

(ii) 3D Long wavelength tomography

Seismic tomography provides a snapshot of the present-day state of the mantle, with numerous models developed since the 1980s. While these typically differ in detail, especially for V_p, the long-wavelength (e.g. spherical harmonic degree $\lesssim 12$) isotropic V_s structure has been consistently imaged by different studies (for a review see e.g. [45]). The strength of V_s anomalies depends primarily on the temperature variations in the mantle, which in turn depends on many factors such as mantle viscosity structure, core-mantle boundary (CMB) temperature and internal heating rates. The observed pattern and amplitude of V_s anomalies can thus be used to test several parameters of the MCM.

Due to uneven data coverage and imposed regularisation, tomographic models of the Earth have limited and spatially-variable resolution. To compare the high-resolution, predicted seismic structure of our MCM with published tomographic models, we must therefore adjust the predicted seismic structure using the resolution operator from existing tomography models. Alternative approaches for tomographic filtering include the generalised inverse projection method [46]. While some studies allow for separate filtering of V_p and V_s [47], tomographic studies do not consistently image the V_p structure. Here, we use tomography model S40RTS [48], which has often been utilised in comparisons with geodynamic simulations (e.g. [4]) and for which a tomographic filter is available. The MCM is first re-parameterised in the same parameterisation as the tomographic model [40], e.g. spherical harmonic coefficients up to degree 40 across 21 radial splines [49], before the resolution operator is applied.

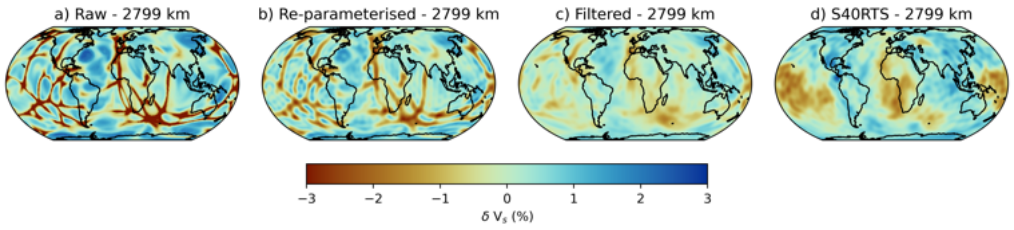

Figure 3. Example of tomographic filtering of a MCM. a) High-resolution δV_s at 2799 km depth from MCM simulation. b) Re-parameterised δV_s up to spherical harmonic degree 40. c) Filtered δV_s using the resolution operator for tomography model S40RTS. d) Seismic tomography model S40RTS.

After filtering, the predicted seismic velocity structure can be compared quantitatively to the tomography model itself. Such comparisons could focus on particular regions or depths, but the exact location of seismic velocity anomalies may differ, e.g. differences in reference frames of plate reconstructions [50]. It is therefore more useful to compute the correlation at each spherical harmonic degree, which indicates whether the structures are of similar wavelengths and at similar locations for relevant depths. We note though that strong correlation does not require similar amplitude. An example of this is given in Fig. 4, where we also show the total correlation for each radial layer up to spherical harmonic degree 8 and 20. A strong positive correlation between S40RTS and the predicted structure of the MCM is found throughout the lower mantle up to spherical harmonic degree 4–5, while the correlation in the upper mantle is higher on average. We also condense the correlation spectra into a single number by computing the weighted mean correlation, accounting for the change in area with depth. For the simulation presented here, the volume weighted mean correlation with S40RTS up to degree 40 is 0.35. This compares favourably to the critical value at a 99% significance level ($r_{crit} = 0.014$). Such weighted mean correlation values can be used as a metric to rank a range of simulations to a given tomography model, in order to assess their relative success in reproducing global seismic structure. This analysis can be performed for the entire mantle, or separately for different depth regions. It can also be extended

to V_p, e.g. using the SP12RTS filter [47]. This would also make it possible to investigate ratios and correlations of seismic velocities, which inform about phase transitions in the mantle.

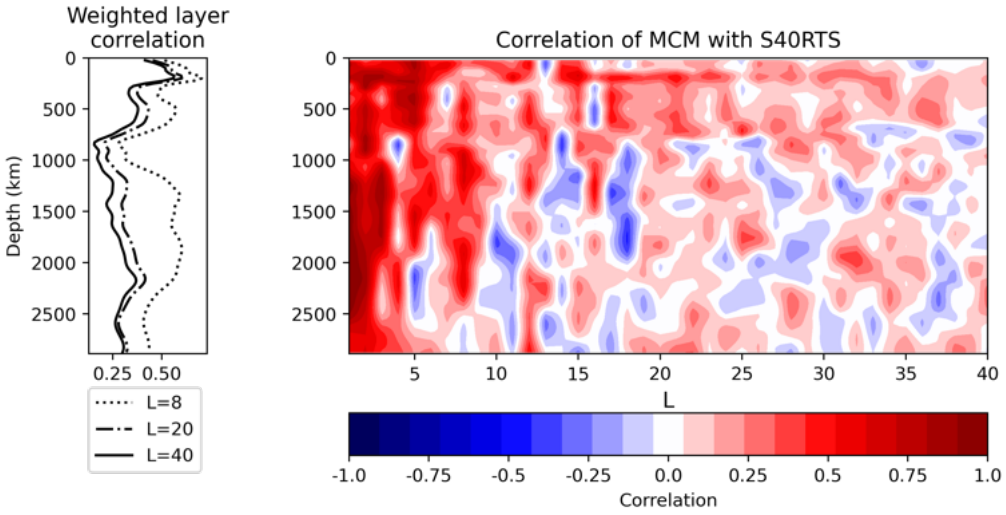

Figure 4. Comparison of the MCM with seismic tomography. Left panel: Total correlation between the filtered, predicted V_s structure of the MCM and seismic tomography model S40RTS, up to spherical harmonic degree $l_{max} = 8$, $l_{max} = 20$ and $l_{max} = 40$. Right panel: Correlation per degree up to degree 40 as a function of depth.

(iii) Normal mode splitting

Earth's normal modes are standing seismic waves that arise after large earthquakes. Their resonance frequencies are affected by Earth's rotation, ellipticity and internal structure, including 3D variations in seismic velocities and, crucially, density [51]. Observations of lateral variations in resonance frequencies (so called splitting function maps) thus provide a way to assess several aspects of the MCMs, albeit only on long wavelengths, e.g. [52]. We illustrate the constraints that normal modes provide by comparing synthetic splitting function maps predicted by the MCM with observations from [53,54] for two groups of modes with specific sensitivity: 10 fundamental modes that are sensitive to the upper mantle and 10 Stoneley modes that are increasingly sensitive to the deepest mantle (see SM). For upper mantle modes (black dots in Figure 5), the MCM prediction matches the observation reasonably well, both in amplitude and pattern (quantified by the correlation and amplitude ratio). However, for lower mantle modes (e.g. Figure 5a–b), the splitting function maps feature similar high frequency anomalies (typically interpreted as cold mantle, downwellings), but the low frequency regions (hot mantle, upwellings) are typically shifted with respect to the observations, resulting in a lower correlation. Although we only analyse 10 modes in each group, this difference is more apparent for lower mantle (blue dots) than for upper mantle (black dots) modes (see Figure SM.2). This suggests that besides assessing the overall mantle structure, normal mode splitting is also a good test for the plate motion history model used in geodynamic simulations [55].

(b) Upper mantle

The upper mantle is studied more widely and better constrained seismically, and many different observations exist that might be used to constrain MCMs. Here, we will consider 1D radial

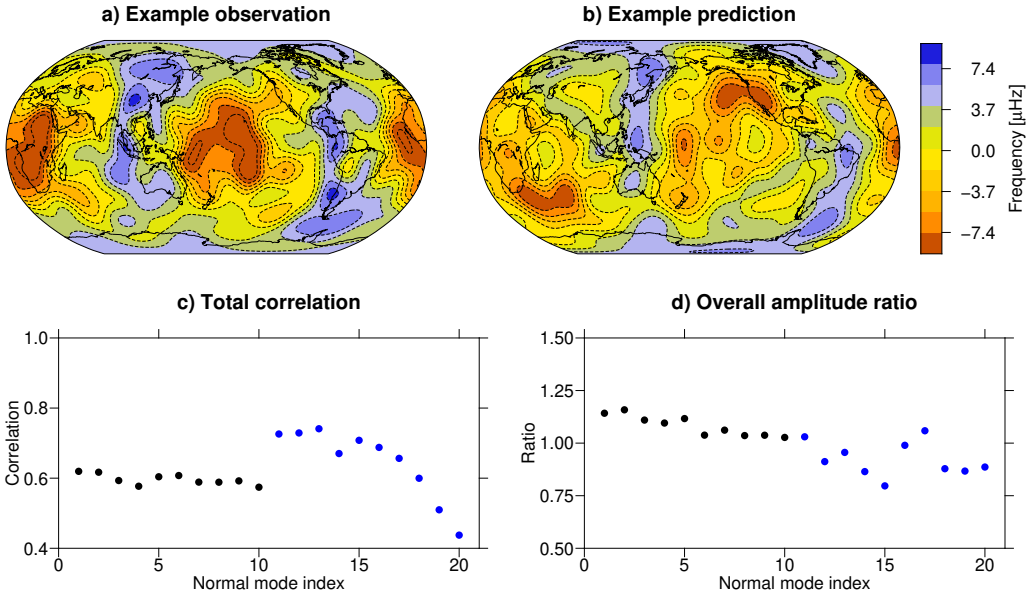

Figure 5. Quantitative assessment of the MCM using normal mode splitting. a) shows the observed splitting function map for lower mantle spheroidal mode ${}_1S_{10}$ with the MCM prediction for the same mode shown in b). c) and d) indicate the total spectral correlation and spectral amplitude ratio for 10 upper mantle modes (black circles) and 10 lower mantle modes (blue circles). These are always computed up to the maximum spherical harmonic degree of the observed splitting function map.

anisotropy, phase velocity maps and SOLA surface wave tomography to illustrate the use of both indirect data and tomography.

(i) 1D radial anisotropy

Seismic velocity structure as discussed above provides a snapshot of the final state of the model. However, in principle, two MCM runs could have very different histories of flow but converge to the same thermal and compositional structure at the present day, resulting in the same isotropic structure. Seismic anisotropy in the mantle is believed to be controlled by the history of deformation (e.g., [56]), so may be an effective discriminant between MCMs with different pasts (e.g., [57]). However, the prediction of seismic anisotropy from MCMs is computationally challenging compared to the prediction of the isotropic signal, and there are additional assumptions behind both the calculation of model values, and results obtained from observation. Seismic anisotropy has been observed (at least regionally) across the whole depth range of the mantle (e.g., [56]), but here we restrict ourselves to the upper 400 km of the mantle. This has the advantage of having the best established mineralogical behaviour, and a well-studied radial anisotropy (both in one and three dimensions). The simplest comparison is the average variation with depth of (shear-wave) radial anisotropy. This captures the general character of the shallow flow field without focussing on regional detail, and is readily compared with a 1D (e.g., PREM [41]) or averaged 3D (e.g., [58–60]) model. In order to calculate the radial anisotropy associated with an MCM, we have assumed upper mantle anisotropy is dominated by the formation of crystallographic preferred orientation in olivine and extended the approach described in [61–67]. Further details are given in the SM section 3.2.1. This approach results in a model of the elastic structure of the upper mantle described by 21 independent elastic constants at each location. For comparison with observation we reduce this to radial anisotropy and focus on the S-wave anisotropic parameter ξ $(= (V_{\mathrm{SH}}/V_{\mathrm{SV}})^2)$.

The global radial variation of ξ for our example MCM is shown in Figure 6. This is evaluated at each 50 km depth interval by averaging 162 evenly laterally distributed points. The comparison with observation (in this case with PREM [41], STW105 [68] and SGLOBE_rani [60]) shows that the shear-wave radial anisotropy has the same sense (i.e., $V_{\mathrm{SH}} > V_{\mathrm{SV}}$) and similar magnitude as that measured for the Earth. This is consistent with an upper mantle dominated by horizontal flow, and lattice-preferred alignment of olivine and enstatite. However, for the tested MCM the anisotropy magnitude peaks much deeper than for the Earth (~250 km, rather than in the upper 150 km). As demonstrated in Figure 6, this is a consequence of the shallow viscosity structure of the example MCM that acts to concentrate strain below the thick high-viscosity lid and also the effects of anisotropy 'frozen' in deep cratonic roots on the reference models. Models for which an Earth-like shallow flow regime is a priority would need to include a much thinner high viscosity 'lithosphere' so that strain is concentrated at shallower depths. Additionally, we have not included here the effect of tomographic filtering (e.g., [69]), which would be needed for more quantitative comparison.

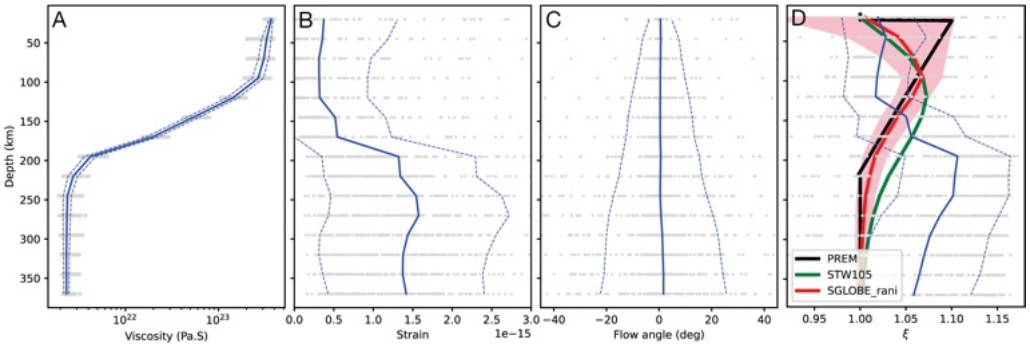

Figure 6. Depth-averaged radial anisotropy predicted by the example MCM. Panels A–C show the most relevant parameters to the generation of upper mantle anisotropy for the final timestep of the model (using [70]). The imposed viscosity structure (Panel A) in the uppermost mantle comprises a high viscosity lid, with a two orders of magnitude reduction occurring between 70–220 km. The lid surface is driven by the imposed plate velocities. The greatest vertical gradient in velocity – and hence strain – occurs in the lower viscosity region peaking around 250 km (Panel B). The model is dominated by horizontal flow (flow angle equals zero) throughout the upper mantle (Panel C). Panel D shows the predicted radial shear-wave anisotropy (ξ, blue line) associated with this flow structure, compared to a global averages from PREM [41] (black line) and STW105 [68] (green line), and average and standard deviation from SGLOBE_rani ([60], red line and pink shading, respectively). In all panels grey dots show the individual points where the model is evaluated, the solid blue line shows the average and the dotted lines the standard deviation for the MCM. It is clear that while this MCM predicts $\xi > 1$ – and a comparable magnitude – of radial anisotropy, it is much deeper than observed.

If the detail of shallow mantle flow is the objective of the model, then comparisons with upper mantle anisotropy can be extended. Three-dimensional tomographic models of radial anisotropy (e.g., [58–60]) could be compared globally or regionally depending on the target of interest. The assumption of radial anisotropy could be relaxed, and a more general azimuthal style of anisotropy could be compared with models derived from surface waves (e.g., [71,72]) or SKS/SKKS phases (e.g., [73]) for better resolution of the flow, at the cost of accounting for significantly more parameters.

(ii) Phase velocity maps

Surface waves provide the strongest constraints on upper mantle structure. We can thus test the global upper mantle structure of the MCMs using both measurements (e.g., phase velocity maps)

and tomography models (discussed in the next section). In either case, it is vital to have a good handle on the data uncertainties.

Here, we build global fundamental mode phase velocity maps up to degree ∼40 using the phase velocity data obtained by [49]. This dataset includes ∼13M measurements that cover 17 period bands (38-275 s). Since depth sensitivity increases with period, our data are sensitive to the whole uppermost mantle down to ∼300 km (see Fig. SM6). Data errors are estimated using a cluster analysis, the inversions are weighted using ray path density and model errors are computed from the model covariance matrix (for details about the inversions see SM section 3.2.2).

We use MINEOS [74] to predict phase velocity maps using a series of 1-D profiles extracted from the MCM on a $2\times2^\circ$ grid. We use all the 17 period bands for which real data are available and fix the crust to CRUST1.0 [75]. This ensures that realistic crustal properties are used in the comparisons. A tomographic filter (see Section 4(a) ii) obtained using the real phase velocity maps is applied to the predicted maps in order to account for the ray coverage, parameterisation and the regularisation applied. This allows us to calculate a quantitative misfit between the real and predicted phase velocity maps at each period; see SM for details.

Comparisons of the predicted MCM phase velocity maps with the observed seismic phase velocity maps are shown in Figure 7. We compute overall misfits for each map and for all wave periods (Fig. 7e), as well as geographically for T∼ 50 s, T∼ 100 s and T∼ 150 s (Fig. 7d). The overall misfit plot (Fig. 7e) shows a general trend of decreasing misfit with increasing wave period, thus indicating the largest differences between the models occur in the shallow mantle (see Fig. SM6 with sensitivity kernels showing that the sensitivity depth increases with increasing period.). This may be due to limitations in CRUST1.0 as well as in the shallow structure predictions from the plate model used to build the MCM. Moreover, Fig. 7e) also shows the largest misfits along major subduction zones. This could be due to the simplified lithosphere or limitations in the modelling of the shallow subduction in the MCM, which will be further discussed in the next section. Further, we emphasise that the main purpose of this study is to provide a tool to test MCMs, with the MCM used being just an illustrative example.

Whilst Figure 7 shows comparisons to fundamental mode Rayleigh phase velocity maps, the analysis can be further extended in future work to include comparisons with overtones. Overtones have greater sensitivity with depth, allowing us to investigate mid-mantle structure (down to ∼660 km depth). Further comparisons can also be made with Love wave phase velocity maps, which have a different sensitivity, and to group velocity maps.

(iii) Surface wave tomography

Seismic data collected in oceanic regions are noisy and have poor coverage. This leads to surface-wave tomographic models with complex 3D resolution and uncertainties. To account for these, here we use the tomographic model *SOLASW3DPacific* [76] built using the SOLA inverse method [77–80] within a finite-frequency framework [81]. The SOLA method provides control over the tomographic resolution (guaranteed to be amplitude bias-free) and uncertainty. By construction, it produces all this information at no extra computational cost. In addition, the finite-frequency framework allows the surface-wave tomography model, and its resolution, to be fully three-dimensional.

Here, we assess the predicted 3D V_{SV} of the MCM in the Pacific upper-mantle. The predicted structure, obtained from the conversion of MCM outputs using mineralogical models described above and initially provided on a very fine grid is interpolated onto the coarser tomographic grid ($2^\circ\times2^\circ$ laterally and 25 km vertically). We apply the SOLA resolution matrix, before we compute the misfit with the data-based tomography model accounting for tomographic uncertainty. Further details are given in the SM, Section 3.3.

Similar to the previous section, we find that away from subduction zones there is good agreement between the MCM prediction and the SOLA model at a depth of 112 km (Figure 8): both show the low-velocity mid-oceanic ridges, high-velocity cratons and a smooth increase of

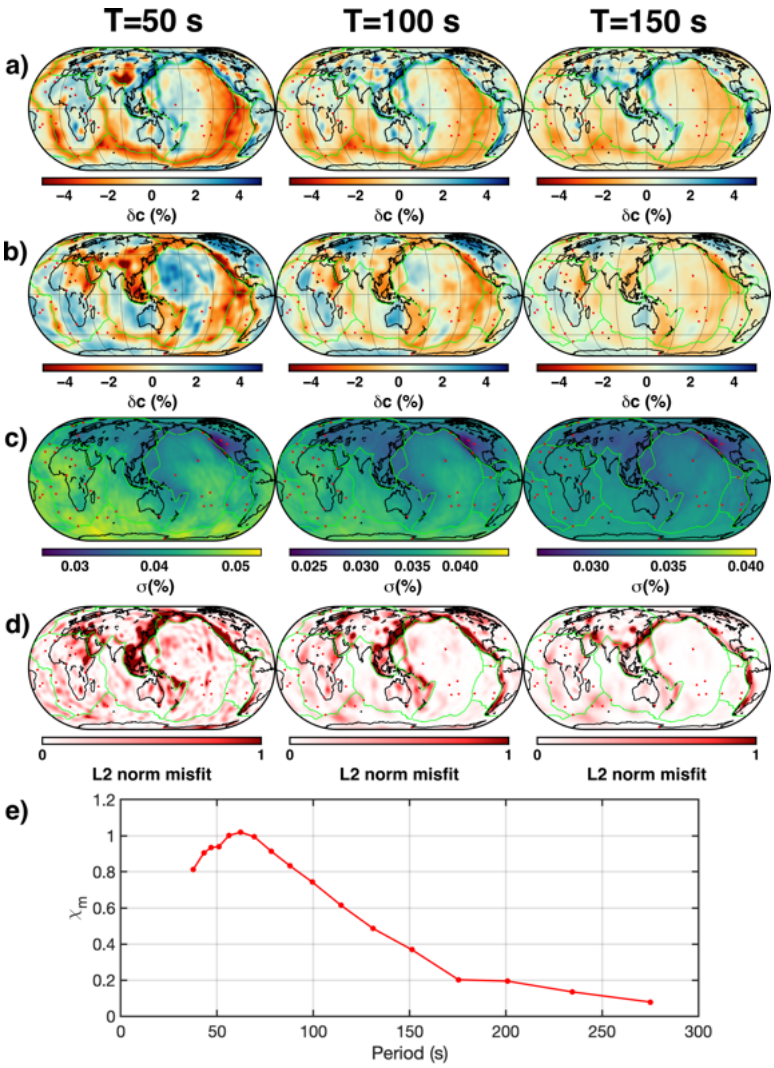

Figure 7. a) Predicted phase velocity perturbations for the example MCM, with a tomographic filter based on the measured phase velocity maps applied. b) Real phase velocity maps from Rayleigh wave measurements. c) Associated phase velocity error maps. d) Geographical L2 norm misfit maps. e) Global misfit as a function of period. All maps are shown at three illustrative periods of 50, 100 and 150 s.

velocity with distance from the ridge. In subduction zones, the agreement is poor: while the MCM predicts high velocities corresponding to plunging slabs, the SOLA tomography model shows low velocities in these regions.

There are several possible explanations for this discrepancy. (i) The lithospheric structure is overly simplified in the MCM – particularly, the ocean-continent dichotomy is not modelled; (ii) slab-induced circulation is not well constrained; (ii) low velocity anomalies at subduction zones in tomography models are often interpreted to be due to hydration melting, [82] a process not modelled in the MCM. (iii) We can perhaps observe the slab signature in SOLA, but it is far weaker than in the MCM. One explanation is that the slabs are too thick in the MCM or, produce too strong anomalies, or do not have the right geometry. Alternatively, this could be due to lateral leakage effects due to the resolution, even if the MCM has been filtered by the SOLA resolution. In the SOLA model, low velocity anomalies due to hydration melting may mask the

the slab signature, but this does not happen in the MCM where hydration melting is not modelled. These discrepancies hold for this specific MCM where the shallow structure appears to be overly simplified. This is a motivation to use more realistic shallow mantle structure in future MCMs and to account for hydration melting.

During these comparisons, we must be aware that the tomographic models are not perfect. Even though we account for their limited resolution and uncertainty, errors due to theoretical approximations are not accounted for [76]. In particular, the strong misfit in Western North America might be explained by non-linear effects not accounted for in the tomography model rather than weaknesses in the MCM. See the SM for other possible seismic constraints.

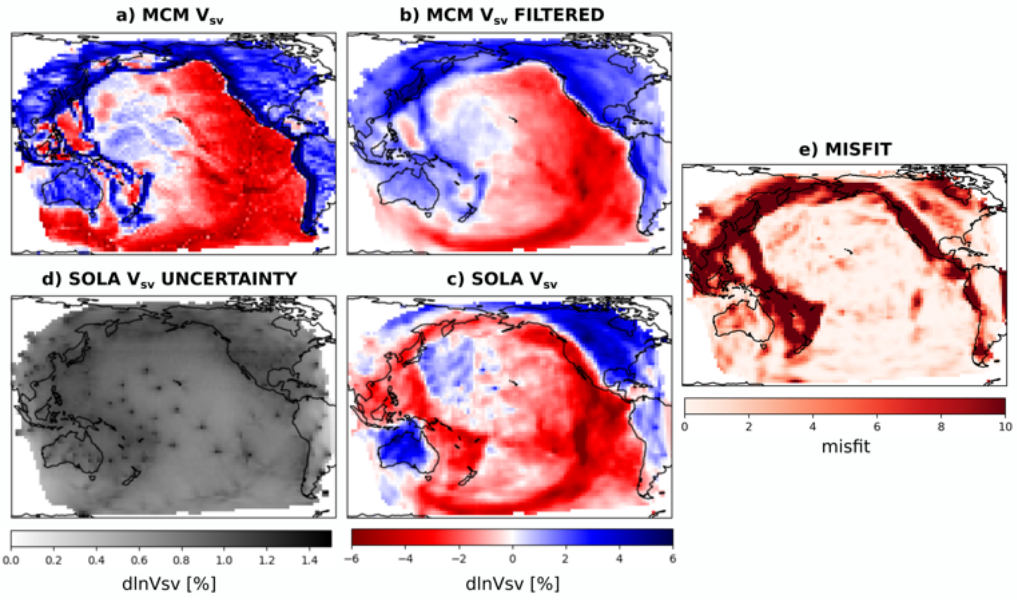

Figure 8. (a) V_{SV} structure predicted by MCM, interpolated onto the tomographic grid, and (b) filtered with SOLA resolution. (c) data-based SOLA V_{SV} tomography model and (d) uncertainty. (e) Misfit (in multiples of SOLA model uncertainty). All maps are at 112 km depth.

5. Testing models with magnetic observations

The geomagnetic field is generated via a dynamo process in the Earth's liquid iron outer core, in which thermal and compositional convection drives motion of an electrically-conducting fluid. The field is thought to have been dipole-dominated for most of its history [83] and undergoes spontaneous polarity reversals, in which the positions of the north and south magnetic poles are swapped over a period typically lasting thousands of years [84]. The reversal frequency has varied from the present day average value of 3-4 reversals every million years, to less than 1 reversal per 10 million years during the Cretaceous Normal Superchron (CNS) and Kiaman Reverse Superchron (KRS), to more than 10 reversals every million years during hyperactive periods such as the mid-Jurassic [85], early Carboniferous [86], and Ediacaran-Cambrian [87].

Several studies have linked variations in reversal frequency to variations in mean CMB heat flux Q, as well as the amplitude and pattern of heat flux heterogeneity [88–95]. The relationship between reversal frequency and CMB heat flux variations is suggested by numerical dynamo simulations. These simulations consistently show that increasing the buoyancy force powering core convection with all other control parameters fixed drives the dynamo from a state in which

the CMB field is strong, dipolar and non-reversing to a state in which the CMB field is weak, multipolar and frequently reversing [96–100]. Dipolar reversals tend to lie near this dipole-multipole transition, suggesting that Earth's core may also lie close in parameter space to this transition [98], thus explaining the periods of both low and high reversal frequency as the field fluctuates between either side of this regime. As explained below, when testing our MCM based on magnetic observations we have investigated Q over the last ~ 300 Myrs, during which time the outer core has had a thick-shell geometry and all of the dynamo control parameters other than buoyancy driving have been essentially constant [101]. Hence, changes in buoyancy (and hence Q) are expected to be the main factor determining the rate of reversals. We would expect changes in Q in our MCM over the last 300 Ma, where short term fluctuations are controlled by variations in the temperature at the CMB, the temperature at the top of the thermal boundary layer, and the thickness of the boundary layer itself.

The direct relation between a given value of Q and a given reversal frequency, or indeed the amplitude of Q at which reversals are induced, is unknown. Ideally, one would consider the connection between CMB heat flux and reversal frequency directly by investigating a MCM coupled to numerical dynamo simulations. However, given that dynamo simulations cannot be ran at the physical conditions of Earth's core and that multiple computationally-expensive simulations would be required to simulate different times in Earth's history predicted by a single MCM, such an investigation would require its own systematic study. We seek criteria that can be applied to any MCM and therefore base our constraining observation solely on the fact that higher Q generally corresponds to more reversals, with periods of high reversal frequency caused by high Q, and periods of low reversal frequency caused by low Q. Comparing Q in our MCM to the reversal frequency inferred from paleomagnetic observations can be hence used to constrain lower mantle heat flow over time (Fig. 1).

Since both the heat flow and reversal frequency are not well constrained, rather than calculating a correlation coefficient in the manner of Choblet *et al.* [102], we instead consider the variation of heat flow properties averaged over the present-day (P, 0-25 My), the mid-CNS (CNS, 90-110 My), and the mid-Jurassic (J, 150-170 My). Although future work could use the methodology proposed in this paper to better constrain the heat flux at the CMB, current estimates range from 5-15TW and as such we do not put any emphasis in our criteria on the value of the heat flux itself, instead comparing the ratios of the average heat flow over the aforementioned time periods. Heat flow should be higher at present-day and during the Jurassic than during the CNS, and as such a mantle circulation model should satisfy the ratios

$$Q_P/Q_{CNS} > 1 \text{ and } Q_J/Q_{CNS} > 1, \tag{5.1}$$

indicating that over the past 170 My the heat flow declined and then rose again. When applying our chosen ratios to the mantle circulation model, we find that $Q_P/Q_{CNS} = 0.988$ and $Q_J/Q_{CNS} = 0.962$ giving the model a score of 0 out of 2 for this criterion.

While not part of our criteria, we also consider the amplitude of the CMB heat flux heterogeneity $Q^* = (Q_{max} - Q_{min})/2Q$, since larger Q^* indicates locally stronger core convection that could induce reversals, and hence we would expect $Q*$ to satisfy the same ratios as Q. For the MCM considered here the time-averaged Q^* is higher during the CNS compared to the Jurassic and present-day, and hence would not satisfy any criteria based on ratios of Q^*. Q^* does not significantly vary throughout the 170 My (with a standard deviation of 0.03 compared to that of 0.18 for Q), indicating it may not be particularly useful for verifying the validity of this model regardless of the ratios.

We also investigated the evolution of the spherical harmonic component Y_2^0, where positive and negative values correspond to large equatorial and polar heat flux respectively. Equatorial cooling is thought to induce reversals even if Q is low [103], while enhanced polar flux stabilises the dipole [90], hence Y_2^0 would ideally be negative during the CNS and positive during the Jurassic and present-day. We find for this model that Y_2^0 is negative throughout the period from

170 My to present, with the dipole most stabilised during the CNS, indicating that there is no increased equatorial heat flux that would influence the reversal frequency in this case.

We chose to use only the ratios Q_P/Q_{CNS} and Q_J/Q_{CNS} for our geomagnetic metrics as plate tectonic models are better constrained from 170 My onwards, leading to the exclusion of ratios involving the KRS. For this model, if we were to consider the heat flux during the Kiaman Q_{KRS} (averaged over 312-262 Ma), we find that $Q_P/Q_{KRS} = 1.031$ and $Q_J/Q_{KRS} = 1.004$. This is in contrast to the CNS ratios. Another ratio that could be considered is Q_J/Q_P, which given the reversal hyperactivity during the Jurassic we would also expect to be greater than one. We chose to omit this ratio from the geomagnetic criteria to focus on solely whether Q falls before then rising after the CNS. We find $Q_J/Q_P < 1$ and hence would not result in this model getting a higher rating if we did choose to consider three ratios rather than two.

6. Testing models with dynamic topography and geoid observations

(a) Observations

A variety of independent estimates of Earth's surface and core-mantle boundary (CMB) deflections can be used to test predictions from mantle circulation models. Since the simulations we examine, like many others, incorporate forcing by horizontal plate motions, we focus on comparing predicted vertical deflections at Earth's surface, h. Arguably the most direct observational evidence for vertical motion induced by mantle convection arise from residual oceanic age-depth measurements, observations of uplifted marine rock and subsidence patterns that cannot be explained by tectonic (e.g. shortening, extension, flexure), glacio-eustatic or sedimentological processes, see e.g. [8,9,104] and references therein. A variety of other indirect estimates including uplift histories from inverse modelling of geomorphic geometries, hiatus mapping and geochemical palaeoaltimetry can also provide information about histories of surface deflections generated in response to mantle convection, e.g. [105–107] (schematically represented in Fig. 1). This summary of observations is necessarily very brief; the interested reader is directed to [9], [8], and [108] for a more detailed introduction to the topic. Independent estimates of dynamic topography at the CMB are more equivocal and we do not explore them further in this contribution, see e.g. [109].

It is straightforward to compare deflections predicted by different simulations. In the following section we first summarise methodologies we have used to generate predictions of dynamic topography from mantle circulation models, with a focus on aiding comparison to a variety of observations and predictions. We then summarise approaches used to assess similarities and differences between predicted surface deflections and independent estimates. An extended description of these methodologies and associated mathematics are provided in the SM.

(b) Testing predictions

Perhaps the harshest test of surface deflections predicted by a mantle convection simulation is to calculate Euclidean (e.g. root-mean-squared, χ; see Equation 16 in SM) misfit between the predicted surface (or derived quantities, e.g. rates of change) and independent estimates. Surface deflections, h, can estimated from MCMs by requiring normal stresses to be continuous across the upper boundary of the solid Earth and the (assumed) overlying fluid with density ρ_w, such that $\sigma_{rr} + \rho_m g_s h = \rho_w g_s h$, where σ_{rr} incorporates the deviatoric viscous stresses generated by mantle convection and dynamic pressure, ρ_m is mean density of the surficial layer of the model, and g_s is gravitational acceleration at Earth's surface, see e.g. [110,111]. Once armed with such estimates of surface deflections it is straightforward to compare them to independent (gridded or spot) estimates, e.g. [104,112]. However, such estimates tend to be extremely sensitive to noise and misalignment, see e.g. [113]. We might, instead, be interested to know whether a simulation predicts surface deflections with broadly the correct frequency content. For instance, it might be useful to know if a simulation has broadly the correct number of upwellings and downwellings

at the correct scale. By transforming surface deflections into the spherical harmonic domain, predictions and independent estimates can be compared at appropriate scales and their power spectra can be assessed, see e.g. [8,114].

An alternative approach is to calculate surface deflections using the analytic propagator matrix technique. This approach requires the generation of sensitivity kernels that relate density anomalies in the mantle to surface deflections, see e.g. [111,115,116]. The kernels principally depend upon (radial) viscosity and boundary conditions. A fuller mathematical description is given in SM. There exists a variety of methodologies to establish similarities and discrepancies of predicted surface deflections with independent estimates once surface deflections are in the frequency domain. First, the degree correlation spectrum, r_l, provides estimates of correlation between independent estimates of dynamic topography and predictions from simulations for each spherical harmonic degree, l, see Equation SM.17 in SM, [11]. It is straightforward to calculate the mean value, i.e. $\overline{r}$. Secondly, the correlation of the entirety of the two fields being compared can also be straightforwardly estimated in the frequency domain, r, see Equation SM.18, [11]. This metric is not, however, sensitive to the amplitudes of the fields. Finally, once armed with spherical harmonic representations of the fields being compared it is straightforward to generate and compare their power spectra, ϕ, or compare power spectra to other independent estimates, e.g. Kaula's rule, see Equation SM.19 [8].

It is also straightforward to compare the geoid predicted from MCMs and independent estimates. Similar to the treatment of dynamic topography, these comparisons are performed in the frequency domain. The geoid is estimated by combining the calculated density structure from the MCM with a geoid sensitivity kernel (see SM). We assume free-slip boundary conditions at the surface and CMB (i.e. vertical velocities = 0, horizontal velocities are free to vary). The degree correlation, correlation of the entire fields, and power spectra can now be calculated to compare the predicted geoid with independent estimates, e.g. from satellite altimetry. Here we compare results to EIGEN-5C [117,118].

(c) Results and suggested improvement

While in principle the topography comparisons can be done over recent geological history, we focus here on comparisons at present day. Figure 9 shows surface deflections calculated using present-day densities predicted by the MCM and the propagator matrix technique to compared independent estimates of dynamic topography up to degree 30. It summarises the assessment of their similarities and differences. χ_p annotated in panel c was calculated by comparing surface deflections predicted using the entirety of the MCM domain (i.e. from the CMB to the surface), Kaula's rule (thin grey curve) and an estimate of residual topography from [8]. In these examples we assume that the fluid overlying the solid Earth is water with $\rho_w = 1030\,\mathrm{kg\,m^{-3}}$. The associated values for models in which the uppermost 100 km (dashed) and 300 km (dotted) of the model domain are excised are $\chi_p = 8.7$ and $\chi_p = 7.2$, respectively. These results, combined with visual inspection of panels a and b, demonstrate that surface deflections from the MCM tend to over-estimate independent estimates of dynamic support by at least an order of magnitude even when the uppermost 100 km of the model domain is excised. Increasing the depth of excision to 300 km brings calculated power spectra nearer to that of oceanic age-depth residuals, but it over-steepens the spectral slope. Consistent with these results, histograms showing the distribution of amplitudes, calculated χ and correlation coefficients, r, r_l and $\overline{r_l}$ (see annotations on figure) emphasise a lack of similarity between the models at nearly all degrees. In nearly all places and all scales the MCM tends to have larger (positive and negative) amplitudes than the independent estimates. Similarly, the MCM tends to over-predict the amplitude of the geoid.

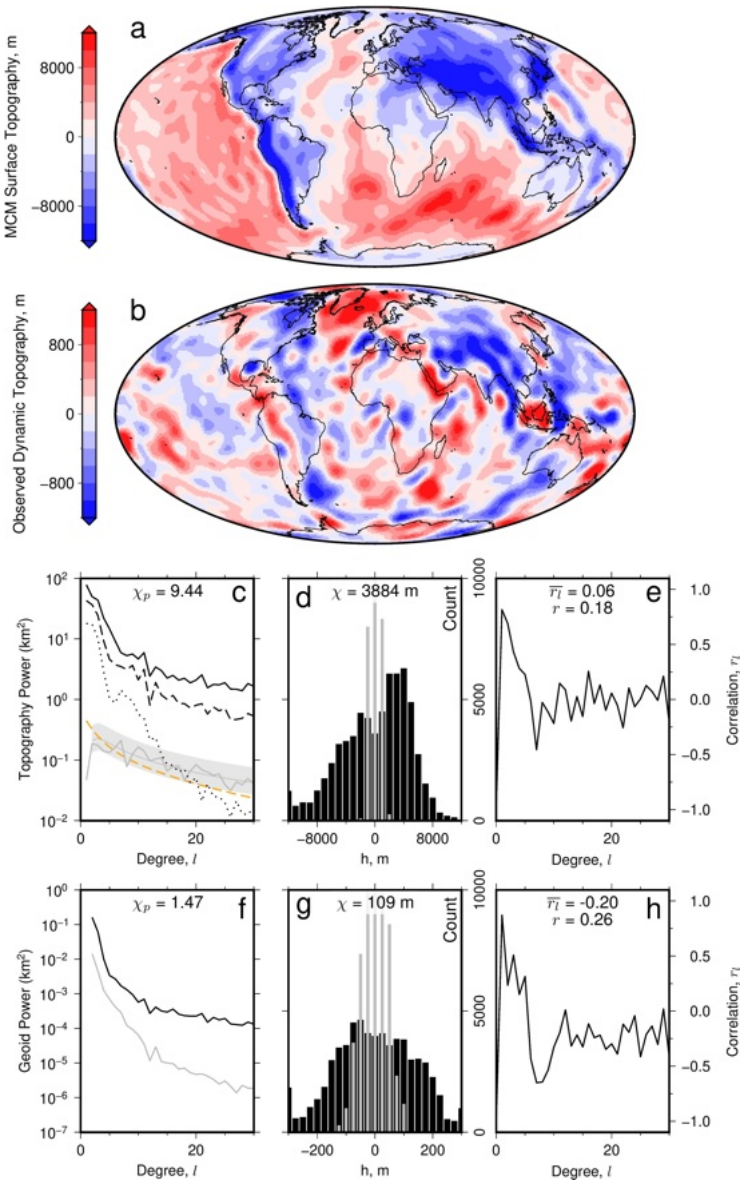

Figure 9. Comparison of modern surface deflections and the geoid predicted by MCM with independent observations up to $l = 30$ (see body text for details). (a) Water-loaded surface deflections predicted by MCM. (b) Calculated residual topography from [114]. (c) Solid black = power spectrum of topography shown in panel a. Dashed & dotted black = spectra when uppermost 100 & 300 km of the MCM are excised, respectively. Thin grey curve and band = expected dynamic topography from Kaula's rule using admittance $Z = 12 \pm 3$ mGal km^{-1}. Thick grey = power spectra of residual topography shown in panel b. Orange dashed = expected power spectra for water-loaded residual topography from [8]. (d) Black/grey = histograms of amplitudes shown in panels a/b. (e) Spectral correlation coefficients, r_l, for panels a and b. (f) Black = power spectrum of geoid calculated using TERRA. Grey = Eigen5c [117]. (g) Black/grey = histograms of geoid amplitudes in MCM/Eigen5c models. (h) Correlation coefficients for MCM/Eigen5c. Note annotated values of χ_p, χ, $\overline{r_l}$ and r are discussed in the body text.

A straightforward addition to this work would be to compare histories of predicted surface deflections and polar wander to independent observations, see e.g. [108,112,119]. There are a number of outstanding challenging issues associated with determining contributions to surface

deflections from the convecting mantle, not least disentangling lithospheric contributions, see e.g. [8,110,120]. It is relatively straightforward to separate deflections generated by loading and flexure of the lithosphere by focusing on deflections at wavelengths longer than even the strongest lithosphere can support elastically, see e.g. [8,121]. Here we consider deflections at spherical harmonic degrees $l \leq 50$, which, at Earth's surface, includes wavelengths, $\lambda \gtrsim 793$ km ($\lambda \approx 2\pi R/\sqrt{l(l+1)}$, where $R \approx 6370$ km is Earth's radius [122]). A much more difficult problem is isolating dynamic support from lithospheric isostasy, see e.g. [123]. A variety of techniques exist to do so, perhaps the most widely used approach is to simply not include the shallowest few hundred kilometers of the model domain in calculations of surface deflections, as we have explored, see e.g. [7,112]. However, that approach can also excise contributions from the shallow convecting mantle, which is undesirable because of surface deflection sensitivity to density anomalies in the uppermost convecting mantle, see e.g. sensitivity kernels in [111,115,116,124], which depend on assumed radial viscosity. Alternative approaches include removal of lithospheric isostatic contributions using independent information about its structure derived from, for instance, shear wave tomographic models [125,126]. Perhaps the most obvious opportunities to improve predicted surface deflections from numerical simulation include allowing surfaces to deform, self-gravitation, development of a probabilistic understanding of mantle circulation and resultant impact on surface deflection uncertainties, and incorporating better understanding of lithospheric structure, especially of lithospheric densities, viscosity, and thermal boundary layer evolution. Many of these issues are actively being addressed, see e.g. [9] and references therein.

7. Testing models with geochemistry and petrology

Three geochemical/petrological metrics are used to rate MCMs: (1) examining how attributes of MCM particles (which track chemistry) beneath ridges and plumes compare with the results of a geochemical model quantifying mantle source parameters from measured mid-ocean ridge basalts (MORB) and ocean island basalts (OIB) radiogenic isotope data (Sr, Nd, Hf, Pb), (2) comparing the Th/U and $^{238}U/^{235}U$ values of MCM particles to modern day measured MORB and OIB values following the recycling of excess U relative to Th and of ^{238}U relative to ^{235}U into the mantle (3) comparing estimates of temperatures of OIB and MORB source regions using petrologic geothermometers versus MCM predictions. It is worth noting that the first two have the ability, in principle, to sense changes over time, while the third is potentially a direct estimate of a driver of mantle circulation, i.e. thermal buoyancy (Fig. 1).

(a) Testing models against a geochemical inversion of MORB and OIB radiogenic isotope data

Evidence for mantle compositional heterogeneities have long been identified from the radiogenic isotope systematics of MORB and OIB (eruptive products of mantle plumes) [127,128]. Systematic isotopic differences require long-lived chemical heterogeneities, consistent with varying extents of radiogenic ingrowth from distinct parent/daughter isotope ratios [129]. The recycling of mafic crustal material into the mantle exerts a primary control on these heterogeneities as it is several orders of magnitudes more concentrated in radioactive and radiogenic trace elements compared to mantle peridotite [130]. On average, OIB show more chemically enriched radiogenic isotope signatures compared to MORB (higher $^{87}Sr/^{86}Sr$, $^{206,207,208}Pb/^{204}Pb$, lower $^{143}Nd/^{144}Nd$, $^{176}Hf/^{177}Hf$), suggesting larger amounts of recycled crust in the source of mantle plumes compared to the mid-oceanic ridge mantle.

Plumes sample the deeper mantle [131] and crustal material is denser than mantle peridotite across most mantle depths [132,133]. The relative enrichment of plumes in crustal material compared to the surrounding mantle sampled by mid-oceanic ridges is quantitatively limited by the buoyancy of ascending crustal material, which can be varied across MCMs by varying the

buoyancy number of the basalt. MCM particles keep track of crustal material circulating in the mantle (through the C attribute). The mean difference in the amount of crustal material between the mantle melting at plumes and ridges in MCMs can therefore be directly compared to the same metric derived from Earth's MORB and OIB radiogenic isotope dataset. This comparison allows evaluating whether assumptions about the buoyancy of crustal material in the MCMs are Earth-like.

Quantifying the enrichment in crustal material of plumes (OIB source) relative to ridges (MORB source) from real MORB-OIB radiogenic isotope data is not straightforward. This is because the amount of crustal material in the mantle is one of many parameters controlling the radiogenic isotope composition of mantle-derived basalts [129,134]. We address this problem in a geochemical model (see details in SM) where we explore the detailed geochemical parameter space of mantle source evolution leading to modern basalts from a primitive mantle source at 4.57 Gyr. Parameters of this model include the extent of peridotite melt-depletion, the amount of crustal material recycled into the mantle, the ages of source modification, the proportion of continental material, and the alteration/dehydration of crustal material. We interpret global radiogenic isotope datasets for MORB and OIB (from the GEOROC and PetDB databases) with this model on a sample-to-sample basis through a *Monte Carlo* approach. Results of our geochemical inversion yield a mean amount of crustal material $f_{RC}^{OIB,Geochem}$ = 7.0% in the OIB source, and $f_{RC}^{MORB,Geochem}$ = 5.7% in the MORB source. This means the difference in crustal material enrichment of the OIB source relative to the MORB source is $\Delta f_{RC}^{Geochem}$ = +1.3%. Note that the mean OIB value is weighted by the buoyancy flux of individual plumes [120] rather than by the number of samples.

To make the same comparison with the MCM we extract the particles present under ridges and plumes active in the MCM at present-day. Particles located right under the melting zones are selected to ensure their C values reflect time-integrated chemistry rather than present-day melting. Particles are associated with a ridge if they lie laterally within 75 km of the ridge axis as it is projected vertically down into the mantle in a depth range of 135-300 km. To identify plumes, we use the plume detection scheme implemented in `terratools` [70] which uses the product of the non-dimensionalized radial velocity and temperature fields (SM Section 5.1). Particles are associated with plumes if they fall within the bounds of any of the identified plumes in depth range of 135-300 km (SM Section 5.1). The f_{RC} value are calculated from the C values of populations of particles (one f_{RC} value per population), using equation SM.23.

Particles under plume melting zones are grouped into a OIB source population yielding $f_{RC}^{\text{OIB,MCM}}$. All particles under ridges are grouped into a MORB source population yielding $f_{RC}^{\text{MORB,MCM}}$. The enrichment in crustal material of plumes relative to ridges $\Delta f_{RC}^{\text{MCM}}$ is then the difference between the two values. The MCM yields a $\Delta f_{RC}^{\text{MCM}}$ of +1.1% with an inter-plumes standard deviation of ±1.2%, thus near-identical to $\Delta f_{RC}^{Geochem}$ = +1.3%.

(b) Testing models with Th/U ratios and U isotopic compositions of mantle derived basalts

Following the onset of the first major rise in atmospheric oxygen across the great oxygenation event (GOE) (~2.3 Ga), there would have been a supply of continent derived U to the oceans due to oxidative weathering. The hydrological recycling of this U relative to Th (which is fluid immobile) from the continental crust into the upper mantle, through subduction, can result in the lowering of the upper mantle Th/U, measured in MORB, faster than the time integrated Th/U ratio calculated from Pb isotopic compositions of MORB [135–137]. The gradual lowering of the Th/U ratio of the upper mantle from chondritic compositions (~3.9) [138] since the GOE to compositions measured in modern day MORB (~2.4-3.8) [139] reflects the pollution of the upper mantle with surface-derived, recycled U (Fig. 10a). Ocean island basalts also show a range in largely sub-chondritic Th/U ratios (~3-4.5), that reflect recycled U, but are typically higher than MORB (Fig. 10a). A positive trend between Pb model ages of OIB sources and their Th/U

ratios [140,141], reflects the continual recycling into lower mantle OIB sources of crust produced from an upper mantle with steadily decreasing Th/U. Therefore, the recycling of U generates distinct patterns in U elemental geochemistry across the mantle that can be used to assess MCMs.

The isotopic behaviour of U also provides a complement to the inferences that can be gained from elemental Th/U. Low temperature isotopic fractionation of U during hydrothermal seawater alteration of the oceanic crust and associated uptake and enrichment of U results in low Th/U and isotopically distinct $^{238}U/^{235}U$ ratios of altered mafic oceanic crust (AMOC), that are on average elevated above chondritic compositions [141] (Fig. 10a). Mid-ocean ridge basalts have low Th/U ratios and higher $^{238}U/^{235}U$ ratios than chondritic compositions that are attributed to the pollution of the MORB source with recycled isotopically distinct AMOC [141] (Fig. 10a). Ocean Island basalt sources however have chondritic $^{238}U/^{235}U$ ratios, which is inconsistent with the modern U cycle [141] (Fig. 10a). Given the redox sensitive nature of U, the high $^{238}U/^{235}U$ ratios of AMOC is a recent feature in Earth's history; the isotopic fractionation during the alteration of ocean crust has likely only occurred since the deep oceans became oxygen rich [141] ($\sim$0.8-0.4 Ga, e.g., [142–145]). Therefore, OIB and MORB sources appear to be differently polluted by recycled oceanic crust, with more and isotopically distinct U returned to the shallow MORB source than deep OIB sources. This is another distinct mantle geochemical parameter that can be used to assess MCMs, and notably the responsible process has a 'known' start time of $\sim$0.8-0.4 Ga, within the time-period of the MCM.

The MCM started with set initial concentrations of U and Th and recycled a set excess flux of U relative to Th into the mantle over 1.2 Gyr of convection, (see [146] for an example of U recycling in MCMs). By monitoring the ratio of ^{232}Th and ^{238}U particles over the timescale of convection we can compare the ratios in plumes relative to those under ridges, to examine how well they reflect present day measured values of OIB and MORB, and the relative differences between the two groups of mantle derived basalts (Fig. 10b). From 0.7 Ga (our chosen time of deep ocean oxygenation) the MCM preferentially recycles 0.02% more ^{238}U relative to ^{235}U, compared to the chondritic Earth value. As a first model, this is done simply, by spreading this excess ^{238}U in the surface particles. This leads to this signature being taken deep into the mantle by subduction, which is how surface particles re-enter the convecting mantle. By comparing the $^{238}U/^{235}U$ ratio of plumes to ridges we can monitor the global distribution of recycled U on an ocean basin scale and compare relative differences to measurements of modern day OIB and MORB (Fig. 10b). However, in the MCM illustrated in (Fig. 10b), the expected first order feature of lower Th/U and higher $^{238}U/^{235}U$ in the upper mantle, as sampled by MORB, relative to the lower mantle, as sampled by OIB, is not observed. This potentially reflects how the excess ^{238}U is recycled. It may need to be returned to the upper mantle past the zone of arc magmatism rather than be subducted into the deeper mantle by slabs, a hypothesis already proposed [141], that can be explored by further modifying the ways in which U is recycled in different MCMs.

MCMs can therefore be assessed by the relative differences in the Th/U and $^{238}U/^{235}U$ ratios of particles in plume and spreading centre regions (which can be done on an ocean basin scale - Atlantic, Pacific, and Indian) and how well they reflect modern mantle compositions based on measurements of modern day OIB and MORB. [141].

(c) Testing models against petrological estimates of mantle potential temperature

With planetary cooling being the driver of all interior dynamics on Earth, it is natural to ask the question of whether geodynamic models are faithful to Earth's observed mantle temperature. The absolute temperature that a geodynamic model will operate at is sensitive to numerous model properties including, but not limited to, the rheology model used, core temperature, internal heating, whether boundary layer behaviour is correctly captured, and the presence and amplitude of compositional density anomalies. As a result, comparison between the absolute temperatures of models and data are unlikely to be fruitful; with model temperature adjusting according to

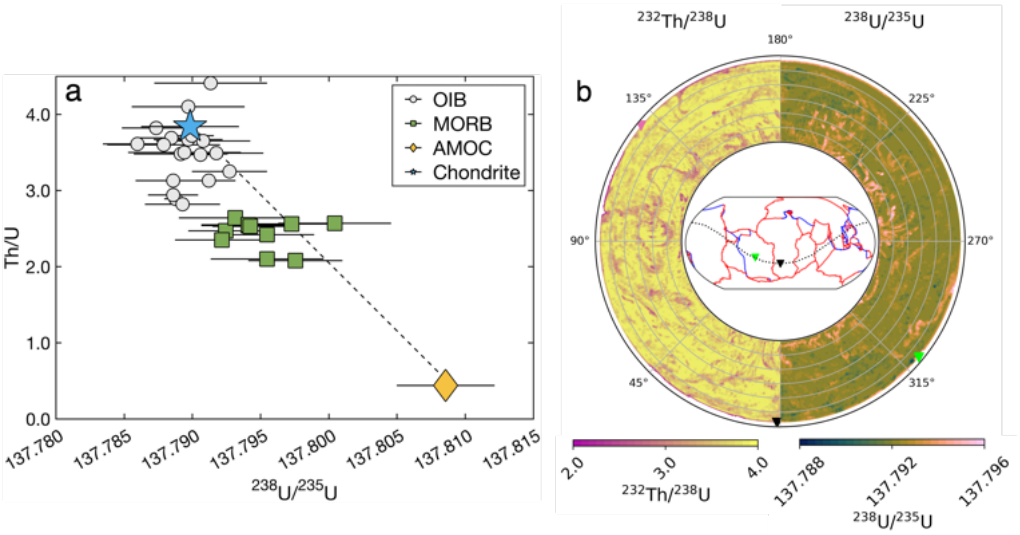

Figure 10. Overview of U elemental and isotopic recycling in MCM runs (a) Uranium isotopic compositions, $^{238}U/^{235}U$, versus Th/U ratio for mantle derived basalts, chondrite, and AMOC. Figure is re-created and modified from [141]. Ocean island basalts (grey circles) have similar $^{238}U/^{235}U$ to chondrite (blue star), while the higher $^{238}U/^{235}U$ and lower Th/U of MORB (green squares) imply a mixture (black dashed line) between chondrite and AMOC (yellow diamond), represented by the Ocean Drilling Program site 801 Supercomposite. Data are from [141] and error bars are the two standard error. Isotopic data has been converted from δ notation to ratios by normalising to a $^{238}U/^{235}U$ ratio of 137.832 [141]. (b) Global cross section for the example MCM following 1.2 Gyr of excess U recycling relative to Th and 0.7 Gyr of excess ^{238}U recycling relative to ^{235}U showing (left section) $^{232}Th/^{238}U$ and (right section) $^{238}U/^{235}U$ at 0 Ma, with an inset map showing red and blue lines for locations of ridges and subduction zones respectively and dotted black line with coloured triangle indicating the direction of the cross-section.

these other parameter choices to regulate internal heating [147–149]. Instead, comparing the distribution of temperature differences within the model and within observations of Earth has the potential to remove some of these systematic offsets and illuminate the more fundamental differences in geodynamic model behaviour versus the Earth.

The natural reference temperature that connects observations and models is that of the 'ambient' mantle. On Earth, this is most readily sampled by petrological thermometers at mid-ocean ridges, where passive plate spreading causes underlying mantle to partially melt. As an MCM has the mid-ocean ridge geometry imposed upon it, then we can take the sub-ridge regions of the model and compare the temperature of these to the temperatures reconstructed from observations.

Petrological thermometers typically do not record mantle temperature directly. We focus on using results from an olivine-spinel exchange thermometer [150,151], applied to natural basalts from mid-ocean ridges and ocean islands (results from [152]). In principle, this thermometer records the temperature at which co-existing olivine and spinel last exchanged aluminium. Given the slow diffusing nature of Al in olivine [153], this last inter-phase exchange of aluminium would have likely occurred shortly after the olivine-spinel pair crystallised from the magma (although see [151] for a discussion of how far this assumption holds). The temperature recorded by this petrological thermometer will be significantly less than the mantle temperature due to [154,155]: magmatic differentiation; adiabatic cooling of the magma during ascent; any super-liquidus cooling the melt experienced; and, cooling of the mantle during decompression melting. By accounting for these effects Li *et al.*, [152] produced estimates of mantle temperature: however, it

is important to note that uncertainty on the mantle temperature estimate is significantly enhanced when acknowledging the uncertain contributions to magma cooling prior to crystallisation [154]. For comparison, we also include a recent compilation of mantle temperatures derived from seismology [156].

MCM temperatures for sub-ridge mantle and mantle plumes are compared with both petrological and seismological mantle temperature estimates in Figure 11. The observations of mantle temperature from both petrological [152] and estimates based on seismic tomography (corrected for tomographic filtering) [156] agree well. The MCM excess plume temperatures are systematically higher than the plume temperature excess observed on Earth by $\sim 200^{\circ}$C on average (Fig. 11 a1 vs. a2). However, comparing the plume temperatures directly, the MCM plumes have a similar variation in temperatures to those found among ocean islands (Fig. 11 b1 and b2). MCM plumes are therefore 'running hot' compared to Earth, but otherwise have the same range of hotter and cooler plumes.

As noted above, absolute model temperatures could be offset from Earth's mantle temperature due to a wide range of model-related factors. Here we have considered relative temperature deviations from ambient mantle to mitigate this, but still find this particular model to have hotter plumes than Earth. Hotter plumes might occur in MCMs from numerous choices made in set up of the simulation: whether the simulation is Boussinesq or fully compressible; the choice of rheology model; the core temperature; the bottom boundary condition, in particular the presence of dense stable piles; magnitude of compositional density anomalies (e.g., from oceanic crustal recycling); and the presence of transition zone phase changes and their associated thermodynamics.

These features of the model and parameters would need to be systematically varied to establish what choices were consistent with Earth's observed plume temperatures. If we are then interested in accurate descriptions of intra-plate melting fluxes and chemical evolution of the mantle driven by these processes, excessively hot plumes sets up a problem that is difficult to solve by adjusting the mantle's melting properties, as that would then dampen ridge melting.

This discrepancy between petrological temperatures and model temperatures highlights the value of a multi-constraint approach to evaluating the fitness of geodynamic models.

8. Summary

We have presented a suite of observations and demonstrated how they can be used to test predictions from mantle circulation modelling. Some of these constraints relate to present-day observations (seismic, surface deflection) and the others to observations over time. Equally, some of the observations are sensitive to properties near the surface (e.g. surface deflection and melting) and others the whole mantle volume. This combination of disparate observations will provide tighter constraints on mantle circulation than any single observation alone.

We remind the reader that when undertaking the comparison one needs to consider the limitations of the mantle circulation model and/or observations - for example we can expect that a detailed crust and lithosphere structure is likely required for a good comparison with surface deflection. We note that we have only presented a sub-set of possible observations that could be used, many others are mentioned in other contributions to this issue. We have also not discussed the possibility of using variational data assimilation with MCMs using adjoint methods (e.g [157,158]) , a powerful extension. Another contribution in this issue will illustrate the power of applying multiple observational constraints simultaneously to a number of models.

The mantle circulation model presented here fits some observations reasonably well (long wavelength lower mantle seismic structure, splitting of normal modes, shallow seismic structure of Pacific basin, spread of temperatures at MOR, differing amount of depletion between OIB and MORB source regions) and others less well (e.g. paleomagnetism, surface deflection, subduction zone seismic structure, upper mantle seismic anisotropy, and U isotopes). This varying misfit suggests that applying such a disparate group of observations will allow much to be learnt about mantle circulation.

Acknowledgements. This research was funded by NERC grants NE/T012633/1, NE/T012463/1, NE/T01248X/2, NE/T012684/1, NE/T012536/1, NE/T012595/1, NE/T012641/1, NE/T012455/1, and

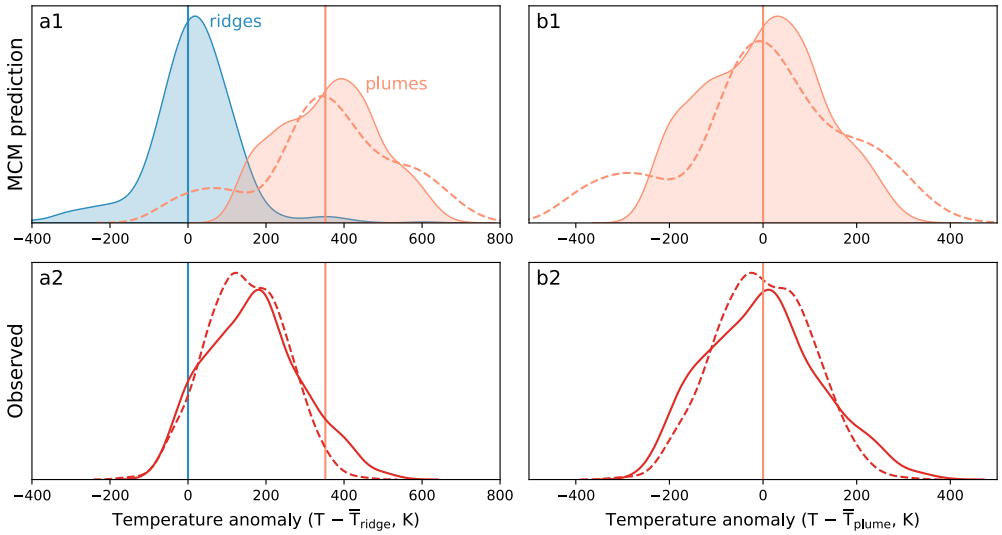

Figure 11. A comparison of MCM plume and ridge temperatures (top: a1, b1) against observed plume temperatures (bottom: a2, b2) from [156], dashed line, and [152], solid line. All temperatures are shown normalised to the ridge average temperature (MCM) or a representative ridge temperature estimate (for observationally constrained estimates). The two plume temperature distributions from the MCM results, one filled and one unfilled with a dashed line, indicate two different approaches to extracting plumes from the model: the dashed line capturing shallow mantle more likely to overlap with shallow ridge segments.

NE/T012501/1 ("MC^2 - Mantle Circulation Constrained"); Royal Society University Research Fellowship (URF180377); NERC DTP project Grant No. NE/S007504/1; and PSE College, Cardiff Uni.. This work used the ARCHER UK National Supercomputing Service (http://www.archer.ac.uk). This is Cardiff EARTH CRediT Contribution 39. For the purpose of Open Access, the authors have applied a CC BY public copyright licence to any Author Accepted Manuscript (AAM) version arising from this submission. We are very grateful for the very extensive suggestions of two anonymous reviewers and the Editor (H.-P.Bunge) which have significantly improved this paper.

Data Accessibility. Simulation data and unpublished code used in this work is available at 10.5281/zenodo.13960492.

References

1. Bunge HP, Richards MA, Lithgow-Bertelloni C, Baumgardner JR, Grand SP, Romanowicz BA. 1998 Time scales and heterogeneous structure in geodynamic Earth models. *Science* **280**, 91–95.
2. Davies JH, Bunge HP. 2001 Seismically "fast" geodynamic mantle models. *Geophys. Res. Lett.* **28**, 73–76.
3. McNamara AK, Zhong S. 2005 Thermochemical structures beneath Africa and the Pacific Ocean. *Nature* **437**, 1136–1139.
4. Davies DR, Goes S, Davies J, Schuberth B, Bunge HP, Ritsema J. 2012 Reconciling dynamic and seismic models of Earth's lower mantle: The dominant role of thermal heterogeneity. *Earth Planet. Sci. Lett.* **353-354**, 253–269. (10.1016/j.epsl.2012.08.016)
5. Bower DJ, Gurnis M, Seton M. 2013 Lower mantle structure from paleogeographically constrained dynamic Earth models. *Geochem. Geophys. Geosys.* **14**, 44–63.
6. Flament N, Williams S, Müller RD, Gurnis M, Bower D. 2017 Origin and evolution of the deep thermochemical structure beneath Eurasia. *Nature Communications* **8**, 14164.

7. Flament N. 2018 Present-day dynamic topography and lower-mantle structure from palaeogeographically constrained mantle flow models. *Geophys. J. Int.* **216**, 2158–2182.
8. Holdt MC, White NJ, Stephenson SN, Conway-Jones BW. 2022 Densely sampled global dynamic topographic observations and their significance. *J. Geophys. Res.: Solid Earth* **127**, 1–32.
9. Hoggard MJ, Austermann J, Randel C, Stephenson S. 2021 Observational Estimates of Dynamic Topography Through Space and Time. In *Mantle Convection and Surface Expressions* , pp. 371–411. AGU. (10.1002/9781119528609.ch15)
10. Hounslow MW, Domeier M, Biggin AJ. 2018 Subduction flux modulates the geomagnetic polarity reversal rate. *Tectonophysics* **742**, 34–49.
11. Forte A, Simmons N, Grand S. 2015 Constraints on 3-D seismic models from global geodynamic observables: Implications for the global mantle convective flow. In Schubert G, editor, *Treatise on Geophysics (2nd Ed.)* , pp. 853–907. Oxford: Elsevier.
12. Schuberth BSA, Bigalke T. 2021 From Mantle Convection to Seismic Observations. In *Mantle Convection and Surface Expressions* , pp. 97–119. American Geophysical Union.
13. Gerya T. 2014 Precambrian geodynamics: Concepts and models. *Gondwana Res.* **25**, 442–463.
14. Bunge HP, Richards MA, Baumgardner JR. 2002 Mantle–circulation models with sequential data assimilation: inferring present–day mantle structure from plate–motion histories. *Phil. Trans. Roy. Soc. Lond. Series A* **360**, 2545–2567.
15. Cao X, Flament N, Müller RD. 2021 Coupled evolution of plate tectonics and basal mantle structure. *Geochem. Geophys. Geosys.* **22**, e2020GC009244.
16. van der Meer DG, van Hinsbergen DJJ, Spakman W. 2018 Atlas of the underworld: Slab remnants in the mantle, their sinking history and a new outlook on lower mantle viscosity. *Tectonophys.* **723**, 309–448.
17. Jones TD, Maguire RR, van Keken PE, Ritsema J, Koelemeijer P. 2020 Subducted oceanic crust as the origin of seismically slow lower-mantle structures. *Progress in Earth and Planet. Sci.* **7**, article number 17.
18. Baumgardner JR. 1985 Three-dimensional treatment of convective flow in the earth's mantle. *Journal of Statistical Physics* **39**, 501–511. (10.1007/BF01008348)
19. Bunge HP, Baumgardner JR. 1995 Mantle convection modeling on parallel virtual machines. *Computers in Physics* **9**, 207–215. (10.1063/1.168525)
20. Bunge HP, Richards MA, Baumgardner JR. 1997 A sensitivity study of three-dimensional spherical mantle convection at 10^8 Rayleigh number: Effects of depth-dependent viscosity, heating mode, and an endothermic phase change. *J. Geophys. Res.: Solid Earth* **102**, 11991–12007.
21. Davies DR, Davies JH, Bollada PC, Hassan O, Morgan K, Nithiarasu P. 2013 A hierarchical mesh refinement technique for global 3-D spherical mantle convection modelling. *Geoscientific Model Development* **6**, 1095–1107. (10.5194/gmd-6-1095-2013)
22. Van Heck HJ, Davies JH, Elliott T, Porcelli D. 2016 Global-scale modelling of melting and isotopic evolution of Earth's mantle: Melting modules for TERRA. *Geoscientific Model Development* **9**, 1399–1411. (10.5194/gmd-9-1399-2016)
23. Müller RD, Flament N, Cannon J, Tetley MG, Williams SE, Cao X, Bodur OF, Zahirovic S, Merdith A. 2022 A tectonic-rules-based mantle reference frame since 1 billion years ago – implications for supercontinent cycles and plate–mantle system evolution. *Solid Earth* **13**, 1127–1159. (10.5194/se-13-1127-2022)
24. Davies CJ. 2015 Cooling history of Earth's core with high thermal conductivity. *Phys. Earth Planet. Int.* **247**, 65–79.
25. Davies GF. 2008 Episodic layering of the early mantle by the 'basalt barrier' mechanism. *Earth Planet. Sci. Lett* **275**, 382–392.
26. Yang WS, Baumgardner JR. 2000 A matrix-dependent transfer multigrid method for strongly variable viscosity infinite Prandtl number thermal convection. *Geophys. & Astrophys. Fluid Dyn.* **92**, 151–195. (10.1080/03091920008203715)
27. Stegman DR, Richards MA, Baumgardner JR. 2002 Effects of depth-dependent viscosity and plate motions on maintaining a relatively uniform mid-ocean ridge basalt reservoir in whole mantle flow. *J. Geophys. Res.: Solid Earth* **107**. (10.1029/2001JB000192)
28. Walzer U, Hendel R, Köstler C, Müller M, Kley J, Viereck-Götte L. 2013 A forward model of mantle convection with evolving continents and a model of the Andean subduction orogen. In Nagel WE, et al., editors, *High Performance Computing in Science and Engineering '12* , pp. 473–501. Berlin: Springer.
29. Xu W, Lithgow-Bertelloni C, Stixrude L, Ritsema J. 2008 The effect of bulk composition and temperature on mantle seismic structure. *Earth Planet. Sci. Lett.* **275**, 70–79.

30. Baker MB, Beckett JR. 1999 The origin of abyssal peridotites: a reinterpretation of constraints based on primary bulk compositions. *Earth Planet. Sci. Lett.* **171**, 49–61.
31. Walter MJ. 2003 2.08 - Melt Extraction and Compositional Variability in Mantle Lithosphere. In Holland HD, Turekian KK, editors, *Treatise on Geochemistry* , pp. 363–394. Oxford: Pergamon.
32. White WM, Klein EM. 2014 4.13 - Composition of the Oceanic Crust. In Holland HD, Turekian KK, editors, *Treatise on Geochemistry (Second Edition)* , pp. 457–496. Oxford: Elsevier.
33. Connolly JAD. 2009 The geodynamic equation of state: What and how. *Geochem. Geophys. Geosys.* **10**, n/a–n/a. (10.1029/2009gc002540)
34. Stixrude L, Lithgow-Bertelloni C. 2005 Thermodynamics of mantle minerals — I. Physical properties. *Geophys. J. Int.* **162**, 610–632. (10.1111/j.1365-246X.2005.02642.x)
35. Stixrude L, Lithgow-Bertelloni C. 2011 Thermodynamics of mantle minerals - II. Phase equilibria. *Geophys. J. Int.* **184**, 1180–1213. (10.1111/j.1365-246X.2010.04890.x)
36. Stixrude L, Lithgow-Bertelloni C. 2021 Thermal expansivity, heat capacity and bulk modulus of the mantle. *Geophys. J. Int.* **228**, 1119–1149. (10.1093/gji/ggab394)
37. Goes S, Cammarano F, Hansen U. 2004 Synthetic seismic signature of thermal mantle plumes. *Earth Planet. Sci. Lett.* **218**, 403–419.
38. Maguire R, Ritsema J, van Keken PE, Fichtner A, Goes S. 2016 P- and S-wave delays caused by thermal plumes. *Geophys. J. Int.* **206**, 1169–1178. (10.1093/gji/ggw187)
39. Matas J, Bukowinski MS. 2007 On the anelastic contribution to the temperature dependence of lower mantle seismic velocities. *Earth Planet. Sci. Lett.* **259**, 51–65.
40. Schuberth BSA, Bunge HP, Ritsema J. 2009 Tomographic filtering of high-resolution mantle circulation models: Can seismic heterogeneity be explained by temperature alone?. *Geochem. Geophys. Geosys.* **10**. (https://doi.org/10.1029/2009GC002401)
41. Dziewonski AM, Anderson DL. 1981 Preliminary reference Earth model. *Phys. Earth Planet. Int.* **25**, 297–356.
42. Stixrude L, Lithgow-Bertelloni C. 2024 Thermodynamics of mantle minerals – III: the role of iron. *Geophys. J. Int.* **237**, 1699–1733. (10.1093/gji/ggae126)
43. Kennett BLN, Engdahl ER, Buland R. 1995 Constraints on seismic velocities in the Earth from traveltimes. *Geophysical Journal International* **122**, 108–124.
44. Styles E, Davies DR, Goes S. 2011 Mapping spherical seismic into physical structure: biases from 3-D phase-transition and thermal boundary-layer heterogeneity. *Geophys. J. Int.* **184**, 1371–1378.
45. Ritsema J, Lekić V. 2020 Heterogeneity of seismic wave velocity in Earth's mantle. *Ann. Rev. Earth Planet. Sci.* **48**, 377–401.
46. Freissler R, Zaroli C, Lambotte S, Schuberth B. 2020 Tomographic filtering via the generalized inverse: A way to account for seismic data uncertainty. *Geophys. J. Int.* **223**, 254–269.
47. Koelemeijer P, Ritsema J, Deuss A, van Heijst HJ. 2016 SP12RTS: a degree-12 model of shear- and compressional-wave velocity for Earth's mantle. *Geophys. J. Int.* **204**, 1024–1039.
48. Ritsema J, Deuss A, van Heijst HJ, Woodhouse JH. 2011a S40RTS: a degree-40 shear-velocity model for the mantle from new Rayleigh wave dispersion, teleseismic traveltime and normal-mode splitting function measurements. *Geophys. J. Int.* **184**, 1223–1236.
49. Ritsema J, Deuss A, Van Heijst H, Woodhouse J. 2011b S40RTS: a degree-40 shear-velocity model for the mantle from new Rayleigh wave dispersion, teleseismic traveltime and normal-mode splitting function measurements. *Geophys. J. Int.* **184**, 1223–1236.
50. Shephard GE, Bunge HP, Schuberth BS, Müller R, Talsma A, Moder C, Landgrebe T. 2012 Testing absolute plate reference frames and the implications for the generation of geodynamic mantle heterogeneity structure. *Earth Planet. Sci. Lett.* **317**, 204–217.
51. Woodhouse J. 1985 Inversion for the splitting function of isolated low order normal mode multiplets. *Eos Trans. AGU* **66**, 300.
52. Richards FD, Hoggard MJ, Ghelichkhan S, Koelemeijer P, Lau HC. 2023 Geodynamic, geodetic, and seismic constraints favour deflated and dense-cored LLVPs. *Earth Planet. Sci. Lett.* **602**, 117964.
53. Deuss A, Ritsema J, van Heijst H. 2013 A new catalogue of normal-mode splitting function measurements up to 10 mHz. *Geophys. J. Int.* **193**, 920–937.
54. Koelemeijer P, Deuss A, Ritsema J. 2013 Observations of core-mantle boundary Stoneley modes. *Geophys. Res. Lett.* **40**, 2557–2561.
55. Koelemeijer P. 2014 Normal mode studies of long-wavelength structures in Earth's lowermost mantle. *University of Cambridge*.

56. Mainprice D. 2007 Seismic anisotropy of the deep Earth from a mineral and rock physics perspective. *Treatise in Geophysics* p. 96.
57. Ward J, Walker AM, Nowacki A, Panton J, Davies JH. 2024 The sensitivity of lowermost mantle anisotropy to past mantle convection. *Phys. Earth Planet. Int.* **356**, 107264.
58. Panning M, Lekić V, Romanowicz B. 2010 Importance of crustal corrections in the development of a new global model of radial anisotropy. *J. Geophys. Res.: Solid Earth* **115**, B12325.
59. French S, Romanowicz BA. 2014 Whole-mantle radially anisotropic shear velocity structure from spectral-element waveform tomography. *Geophys. J. Int.* **199**, 1303–1327.
60. Chang SJ, Ferreira AMG, Ritsema J, Heijst HJ, Woodhouse JH. 2015 Joint inversion for global isotropic and radially anisotropic mantle structure including crustal thickness perturbations. *J. Geophys. Res.: Solid Earth* pp. 1 – 23. (10.1002/(issn)2169-9356)
61. Walker A, Forte A, Wookey J, Nowacki A, Kendall JM. 2011 Elastic anisotropy of D″ predicted from global models of mantle flow. *Geochem. Geophys. Geosys.* **12**, Q10006.
62. Nowacki A, Walker AM, Wookey J, Kendall JM. 2012 Evaluating post-perovskite as a cause of D″ anisotropy in regions of palaeosubduction. *Geophys. J. Int.* **192**, 1085–1090.
63. Ammann MW, Walker AM, Stackhouse S, Wookey J, Forte AM, Brodholt JP, Dobson DP. 2014 Variation of thermal conductivity and heat flux at the Earth's core mantle boundary. *Earth Planet. Sci. Lett.* **390**, 175–185. (https://doi.org/10.1016/j.epsl.2014.01.009)
64. Nowacki A, Wookey J. 2016 The limits of ray theory when measuring shear wave splitting in the lowermost mantle with ScS waves. *Geophys. J. Int.* **207**, 1573–1583.
65. Walker AM, Dobson DP, Wookey J, Nowacki A, Forte AM. 2018 The anisotropic signal of topotaxy during phase transitions in D″. *Phys. Earth Planet. Int.* **276**, 159–171.
66. Creasy N, Pisconti A, Long MD, Thomas C, Wookey J. 2019 Constraining lowermost mantle anisotropy with body waves: a synthetic modelling study. *Geophys. J. Int.* **217**, 766–783.
67. Bilton L, Duvernay T, Davies DR, Eakin CM. 2025 PyDRex: predicting crystallographic preferred orientation in peridotites under steady-state and time-dependent strain. *Geophysical Journal International* **241**, 35–57. (10.1093/gji/ggaf026)
68. Kustowski B, Ekström G, Dziewoński A. 2008 Anisotropic shear-wave velocity structure of the Earth's mantle: A global model. *Journal of Geophysical Research: Solid Earth* **113**.
69. Kendall E, Faccenda M, Ferreira AMG, Chang S. 2022 On the relationship between oceanic plate speed, tectonic stress, and seismic anisotropy. *Geophys. Res. Lett.* **49**, e2022GL097795.
70. Panton J, Nowacki A, Myhill R, Ward J, Walker A, Davies H, Wookey J. 2024 terratools v1.1.0. *Zenodo*. (10.5281/zenodo.11506398)
71. Debayle E, Dubuffet F, Durand S. 2016 An automatically updated S-wave model of the upper mantle and the depth extent of azimuthal anisotropy. *Geophys. Res. Lett.* **43**, 674–682.
72. Schaeffer AJ, Lebedev S, Becker TW. 2016 Azimuthal seismic anisotropy in the Earth's upper mantle and the thickness of tectonic plates. *Geophys. J. Int.* **207**, 901 – 933.
73. Walpole J, Wookey J, Masters G, Kendall J. 2014 A uniformly processed data set of SKS shear wave splitting measurements: A global investigation of upper mantle anisotropy beneath seismic stations. *Geochem. Geophys. Geosys.* **15**, 1991–2010.
74. Masters G, Woodhouse J, Freeman G. 2011 Mineos v1. 0.2 [Software]. *Computational Infrastructure for Geodynamics*.
75. Laske G, Masters G, Ma Z, Pasyanos M. 2013 Update on CRUST1. 0—A 1-degree global model of Earth's crust. In *Geophysical research abstracts* vol. 15 p. 2658.
76. Latallerie F, Zaroli C, Lambotte S, Maggi A, Walker A, Koemeleijer P. 2024 Towards surface-wave tomography with 3D resolution and uncertainty. *EarthArXiv*. (https://doi.org/10.31223/X5FM79)
77. Zaroli C. 2016 Global seismic tomography using Backus-Gilbert inversion. *Geophys. J. Int.* **207**, 876–888. (10.1093/gji/ggw315)
78. Zaroli C, Koelemeijer P, Lambotte S. 2017 Toward seeing the Earth's interior through unbiased tomographic lenses. *Geophys. Res. Lett.* **44**, 11–399.
79. Latallerie F, Zaroli C, Lambotte S, Maggi A. 2022 Analysis of tomographic models using resolution and uncertainties: a surface wave example from the Pacific. *Geophys. J. Int.* **230**, 893–907. (10.1093/gji/ggac095)
80. Latallerie F. 2022 *Seismic tomography of plume-like upwellings in the French Polynesia region using Backus-Gilbert inversion*. Theses Université de Strasbourg. Issue: 2022STRAH012.
81. Zhou Y. 2009 Multimode surface wave sensitivity kernels in radially anisotropic earth media. *Geophys. J. Int.* **176**, 865–888. (10.1111/j.1365-246X.2008.04010.x)

82. Stern RJ. 2002 Subduction Zones. *Rev. Geophys.* **40**, 1012. (10.1029/2001RG000108)
83. Biggin AJ, Bono RK, Meduri DG, Sprain CJ, Davies CJ, Holme R, Doubrovine PV. 2020 Quantitative estimates of average geomagnetic axial dipole dominance in deep geological time. *Nature communications* **11**, 6100.
84. Glatzmaier G, Coe R. 2007 Magnetic polarity reversals in the core. *Treatise on geophysics* **2**, 283–298.
85. Tominaga M, Sager WW, Tivey MA, Lee SM. 2008 Deep-tow magnetic anomaly study of the Pacific Jurassic Quiet Zone and implications for the geomagnetic polarity reversal timescale and geomagnetic field behavior. *J. Geophys. Res.: Solid Earth* **113**, B07110.
86. Hounslow MW, Biggin AJ, Cózar P, Somerville ID, Kamenikova T, Sprain CJ. 2024 A hyperactive geomagnetic field in the Late Visean (Early Carboniferous) from the Late Asbian stratotype section in northwest England, UK. *Geochem. Geophys. Geosys.* **25**, e2023GC011282.
87. Levashova NM, Golovanova IV, Rudko D, Danukalov KN, Rudko S, Yu SR, Meert JG. 2021 Late Ediacaran magnetic field hyperactivity: Quantifying the reversal frequency in the Zigan Formation, Southern Urals, Russia. *Gondwana Res.* **94**, 133–142.
88. Glatzmaier GA, Coe RS, Hongre L, Roberts PH. 1999 The role of the Earth's mantle in controlling the frequency of geomagnetic reversals. *Nature* **401**, 885–890.
89. Driscoll P, Olson P. 2009 Polarity reversals in geodynamo models with core evolution. *Earth Planet. Sci. Lett.* **282**, 24–33.
90. Olson PL, Coe RS, Driscoll PE, Glatzmaier GA, Roberts PH. 2010 Geodynamo reversal frequency and heterogeneous core–mantle boundary heat flow. *Phys. Earth Planet. Int.* **180**, 66–79.
91. Zhang N, Zhong S. 2011 Heat fluxes at the Earth's surface and core-mantle boundary since Pangea formation and their implications for the geomagnetic superchrons. *Earth Planet. Sci. Lett.* **306**, 205–216.
92. Olson PL, Christensen UR, Driscoll PE. 2012 From superchrons to secular variation: a broadband dynamo frequency spectrum for the geomagnetic dipole. *Earth Planet. Sci. Lett.* **319**, 75–82.
93. Olson P, Deguen R, Hinnov LA, Zhong S. 2013 Controls on geomagnetic reversals and core evolution by mantle convection in the Phanerozoic. *Phys. Earth Planet. Int.* **214**, 87–103.
94. Olson P, Amit H. 2014 Magnetic reversal frequency scaling in dynamos with thermochemical convection. *Phys. Earth Planet. Int.* **229**, 122–133.
95. Amit H, Olson P. 2015 Lower mantle superplume growth excites geomagnetic reversals. *Earth Planet. Sci. Lett.* **414**, 68–76.
96. Kutzner C, Christensen UR. 2002 From stable dipolar towards reversing numerical dynamos. *Phys. Earth Planet. Int.* **131**, 29–45.
97. Christensen UR, Aubert J. 2006 Scaling properties of convection-driven dynamos in rotating spherical shells and application to planetary magnetic fields. *Geophys. J. Int.* **166**, 97–114.
98. Olson P, Christensen UR. 2006 Dipole moment scaling for convection-driven planetary dynamos. *Earth Planet. Sci. Lett.* **250**, 561–571.
99. Olson PL, Glatzmaier GA, Coe RS. 2011 Complex polarity reversals in a geodynamo model. *Earth Planet. Sci. Lett.* **304**, 168–179.
100. Menu MD, Petitdemange L, Galtier S. 2020 Magnetic effects on fields morphologies and reversals in geodynamo simulations. *Phys. Earth Planet. Int.* **307**, 106542.
101. Driscoll PE. 2016 Simulating 2 Ga of geodynamo history. *Geophys. Res. Lett.* **43**, 5680–5687.
102. Choblet G, Amit H, Husson L. 2016 Constraining mantle convection models with palaeomagnetic reversals record and numerical dynamos. *Geophysical Supplements to the Monthly Notices of the Royal Astronomical Society* **207**, 1165–1184.
103. Amit H, Leonhardt R, Wicht J. 2010 Polarity reversals from paleomagnetic observations and numerical dynamo simulations. *Space science reviews* **155**, 293–335.
104. Fernandes VM, Roberts GG. 2021 Cretaceous to Recent net continental uplift from paleobiological data: Insights into sub-plate support. *GSA Bulletin* **133**, 1–20.
105. Carena S, Bunge HP, Friedrich AM. 2019 Analysis of geological hiatus surfaces across Africa in the Cenozoic and implications for the timescales of convectively-maintained topography. *Canadian Journal of Earth Sciences* **56**, 1333–1346. (10.1139/cjes-2018-0329)
106. O'Malley CPB, White NJ, Stephenson SN, Roberts GG. 2021 Large-Scale Tectonic Forcing of the African Landscape. *J. Geophys. Res.: Earth Surface* **126**, 1–37.
107. Vilacís B, Brown H, Bunge HP, Carena S, Hayek JN, Stotz IL, Wang ZR, Friedrich AM. 2024 Dynamic topography and the planform of mantle convection since the Jurassic inferred from

global continental hiatus maps. *Proceedings of the Royal Society A: Mathematical, Physical and Engineering Sciences* **480**, 20240311.
108. Fernandes VM, Roberts GG, Richards F. 2024 Testing Mantle Convection Simulations With Paleobiology and Other Stratigraphic Observations: Examples From Western North America. *Geochem. Geophys. Geosys.* **25**, e2023GC011381. (https://doi.org/10.1029/2023GC011381)
109. Koelemeijer P. 2021 9. In *Toward consistent seismological models of the core–mantle boundary landscape*, pp. 229–255. American Geophysical Union (AGU).
110. McKenzie D. 1977 Surface deformation, gravity anomalies and convection. *Geophysical Journal of the Royal Astronomical Society* **48**, 211–238. (10.1111/j.1365-246X.1977.tb01297.x)
111. Parsons B, Daly S. 1983 The relationship between surface topography, gravity anomalies and temperature structure of convection. *J. Geophys. Res.* **88**, 1129–1144.
112. Flament N, Gurnis M, Muller RD. 2013 A review of observations and models of dynamic topography. *Lithosphere* **5**, 189–210. (10.1130/L245.1)
113. Taiwo A, Bunge HP, Craig G. 2024 A meteorology approach to assess mantle flow induced dynamic topography using object-based image processing methods. *Physics of the Earth and Planetary Interiors* **351**, 107195.
114. Hoggard MJ, White N, Al-Attar D. 2016 Suppl. Info. for "Global dynamic topography observations reveal limited influence of large-scale mantle flow". *Nature Geosci.* **9**, 1–34.
115. Hager BH, O'Connell RJ. 1981 A Simple Global Model of Plate Dynamics and Mantle Convection. *J. Geophys. Res.* **86**, 4843–4867. (10.1029/JB086iB06p04843)
116. Ghelichkhan S, Bunge HP, Oeser J. 2021 Global mantle flow retrodictions for the early Cenozoic using an adjoint method: Evolving dynamic topographies, deep mantle structures, flow trajectories and sublithospheric stresses. *Geophys. J. Int.* **226**, 1432–1460.
117. Foerste C, Flechtner F, Stubenvoll R, Rothacher M, Kusche J, Neumayer HK, Biancale R, Lemoine J, Barthelmes F, Bruinsma S, Koenig R, Dahle C. 2008 EIGEN-5C - the new GeoForschungsZentrum Potsdam / Groupe de Recherche de Geodesie Spatiale combined gravity field model. In *AGU Fall Meeting Abstracts* vol. 2008 pp. G13A–0626.
118. Chambat F, Ricard Y, Valette B. 2010 Flattening of the Earth: Further from hydrostaticity than previously estimated. *Geophys. J. Int.* **183**, 727–732.
119. Gold T. 1955 Instability of the Earth's axis of rotation. *Nature* **175**, 526–529.
120. Hoggard MJ, Parnell-Turner R, White N. 2020 Hotspots and mantle plumes revisited: Towards reconciling the mantle heat transfer discrepancy. *Earth Planet. Sci. Lett.* **542**, 116317.
121. Watts AB. 2001 *Isostasy and Flexure of the Lithosphere*. Cambridge University Press.
122. Jeans JH. 1923 The propagation of earthquake waves. *Proc. Roy. Soc. Lond. A* **102**, 554–574.
123. Wang Y, Liu L, Zhou Q. 2022 Topography and gravity reveal denser cratonic lithospheric mantle than previously thought. *Geophys. Res. Lett.* **49**, e2021GL096844.
124. Colli L, Ghelichkhan S, Bunge HP. 2016 On the ratio of dynamic topography and gravity anomalies in a dynamic Earth. *Geophys. Res. Lett.* **43**, 2510–2516.
125. Priestley K, McKenzie D. 2013 The relationship between shear wave velocity, temperature, attenuation and viscosity in the shallow part of the mantle. *Earth Planet. Sci. Lett.* **381**, 78–91.
126. Richards FD, Hoggard MJ, White N, Ghelichkhan S. 2020 Quantifying the relationship between short-wavelength dynamic topography and thermomechanical structure of the upper mantle using calibrated parameterization of anelasticity. *J. Geophys. Res.: Solid Earth* **125**, 1–36. (10.1029/2019JB019062)
127. Zindler A, Hart S. 1986 Chemical geodynamics. *Ann. Rev. Earth Planet. Sci.* **14**, 493–571.
128. Stracke A, Willig M, Genske F, Béguelin P, Todd E. 2022 Chemical geodynamics insights from a machine learning approach. *Geochem. Geophys. Geosys.* **23**, e2022GC010606.
129. Stracke A, Bizimis M, Salters VJ. 2003 Recycling oceanic crust: Quantitative constraints. *Geochem. Geophys. Geosys.* **4**, 8003.
130. Sun SS, McDonough WF. 1989 Chemical and isotopic systematics of oceanic basalts: implications for mantle composition and processes. *Geol. Soc. Lond. Spec. Pub.* **42**, 313–345.
131. French SW, Romanowicz B. 2015 Broad plumes rooted at the base of the Earth's mantle beneath major hotspots. *Nature* **525**, 95–99.
132. Ricolleau A, Perrillat Jp, Fiquet G, Daniel I, Matas J, Addad A, Menguy N, Cardon H, Mezouar M, Guignot N. 2010 Phase relations and equation of state of a natural MORB: Implications for the density profile of subducted oceanic crust in the Earth's lower mantle. *J. Geophys. Res.: Solid Earth* **115**, B08202.
133. Ishii T, Kojitani H, Akaogi M. 2019 Phase relations of harzburgite and MORB up to the uppermost lower mantle conditions: precise comparison with pyrolite by multisample cell

high-pressure experiments with implication to dynamics of subducted slabs. *J. Geophys. Res.: Solid Earth* **124**, 3491–3507.
134. Stracke A, Béguelin P. 2024 Basalts record a limited extent of mantle depletion: cause and chemical geodynamic implications. *Geochem. Perspectives Lett.* **32**, 21–26.
135. Tatsumoto M. 1966 Genetic Relations of Oceanic Basalts as Indicated by Lead Isotopes. *Science* **153**, 1094–1101. (10.1126/science.153.3740.1094)
136. Galer SJG, O'Nions RK. 1985 Residence time of thorium, uranium and lead in the mantle with implications for mantle convection. *Nature* **316**, 778–782.
137. Elliott T, Zindler A, Bourdon B. 1999 Exploring the kappa conundrum: The role of recycling in the lead isotope evolution of the mantle. *Earth Planet. Sci. Lett.* **169**, 129–145.
138. Blichert-Toft J, Zanda B, Ebel DS, Albarède F. 2010 The Solar System primordial lead. *Earth Planet. Sci. Lett.* **300**, 152–163. (https://doi.org/10.1016/j.epsl.2010.10.001)
139. Gale A, Dalton CA, Langmuir CH, Su Y, Schilling JG. 2013 The mean composition of ocean ridge basalts. *Geochem. Geophys. Geosys.* **14**, 489–518.
140. Chase CG. 1981 Oceanic island Pb: Two-stage histories and mantle evolution. *Earth Planet. Sci. Lett.* **52**, 277–284. (https://doi.org/10.1016/0012-821X(81)90182-5)
141. Andersen MB, Elliott T, Freymuth H, Sims KWW, Niu Y, Kelley KA. 2015 The terrestrial uranium isotope cycle. *Nature* **517**, 356–359.
142. Canfield DE, Poulton SW, Narbonne GM. 2007 Late-Neoproterozoic Deep-Ocean Oxygenation and the Rise of Animal Life. *Science* **315**, 92–95. (10.1126/science.1135013)
143. Lyons T, Reinhard C, Planavsky N. 2014 The rise of oxygen in Earth's early ocean and atmosphere. *Nature* **506**, 307–315. (10.1038/nature13068)
144. Stolper D, Keller C. 2018 A record of deep-ocean dissolved O2 from the oxidation state of iron in submarine basalts. *Nature* **553**, 323–327. (10.1038/nature25009)
145. Krause AJ, Mills BJW, Merdith AS, Lenton TM, Poulton SW. 2022 Extreme variability in atmospheric oxygen levels in the late Precambrian. *Science Advances* **8**, eabm8191.
146. Panton J, Davies JH, Elliott T, Andersen M, Porcelli D, Price MG. 2022 Investigating influences on the Pb pseudo-isochron using three-dimensional dantle convection models with a continental reservoir. *Geochem. Geophys. Geosys.* **23**, e2021GC010309.
147. Urey HC. 1955 The cosmic abundances of potassium, uranium, and thorium and the heat balances of the Earth, the Moon, and Mars. *Proc. Nat. Acad. Sci.* **41**, 127–144.
148. Davies GF. 1980 Thermal histories of convective Earth models and constraints on radiogenic heat production in the Earth. *J. Geophys. Res.: Solid Earth* **85**, 2517–2530.
149. Korenaga J. 2016 Can mantle convection be self-regulated?. *Science advances* **2**, e1601168.
150. Coogan L, Saunders A, Wilson R. 2014 Aluminum-in-olivine thermometry of primitive basalts: Evidence of an anomalously hot mantle source for large igneous provinces. *Chem. Geol.* **368**, 1–10.
151. Zhang Y, Namur O, Li W, Shorttle O, Gazel E, Jennings E, Thy P, Grove TL, Charlier B. 2023 An extended calibration of the olivine–spinel aluminum exchange thermometer: Application to the melting conditions and mantle lithologies of large igneous provinces. *J. Petrol.* **64**, egad077.
152. Li W, Shorttle O, Maclennan J, Matthews S, Zhang Y, Namur O, Soderman C, Geist D. 2024 Taking the temperature of ocean islands: a petrological approach. *J. Petrol.* **nnn**, nn–nn.
153. Spandler C, O'Neill HSC. 2010 Diffusion and partition coefficients of minor and trace elements in San Carlos olivine at 1,300 C with some geochemical implications. *Contrib. Mineral. Petrol.* **159**, 791–818.
154. Matthews S, Shorttle O, Maclennan J. 2016 The temperature of the I celandic mantle from olivine-spinel aluminum exchange thermometry. *Geochem. Geophys. Geosys.* **17**, 4725–4752.
155. Matthews S, Wong K, Shorttle O, Edmonds M, Maclennan J. 2021 Do olivine crystallization temperatures faithfully record mantle temperature variability?. *Geochem. Geophys. Geosys.* **22**, e2020GC009157.
156. Bao X, Lithgow-Bertelloni CR, Jackson MG, Romanowicz B. 2022 On the relative temperatures of Earth's volcanic hotspots and mid-ocean ridges. *Science* **375**, 57–61.
157. Liu L, Gurnis M. 2008 Simultaneous inversion of mantle properties and initial conditions using an adjoint of mantle convection. *J. Geophys. Res* **113**, B08405.
158. Bunge HP, Hagelberg CR, Travis BJ. 2003 Mantle circulation models with variational data assimilation: inferring past mantle flow and structure from plate motion histories and seismic tomography. *Geophys. J. Int.* **152**, 280–301.